The Astrophysical Journal, 958:93 (23pp), 2023 November 20 https://doi.org/10.3847/1538-4357/ad00b2

A Chandra Study of the NGC 7618/UGC 12491 Major Group Merger at Apogee: Multiple Cold Fronts, Boxy Wings, Filaments, and Arc-shaped Slingshot Tails

M. E. Machacek[1], C. Jones[1], R. P. Kraft[1], W. R. Forman[1], E. Roediger[2], A. Sheardown[2], and J. T. Wan[3]
[1] Center for Astrophysics | Harvard & Smithsonian, 60 Garden Street, Cambridge, MA 02138, USA; mmachacek@cfa.harvard.edu
[2] E.A. Milne Centre for Astrophysics, Department of Physics and Mathematics, University of Hull, Hull HU6 7RX, UK
[3] Division of Physics, Mathematics and Astronomy, California Institute of Technology, 1200 E California Boulevard, Pasadena, CA 91125, USA
Received 2022 December 21; revised 2023 September 28; accepted 2023 October 4; published 2023 November 15

Abstract

Analyses of major group mergers are key to understanding the evolution of large-scale structure in the Universe and the microphysical properties of the hot gas in these systems. We present imaging and spectral analyses of deep Chandra observations of hot gas structures formed in the major merger of the NGC 7618 and UGC 12491 galaxy groups and compare the observed hot gas morphology, temperatures, and abundances with recent simulations. The morphology of the observed multiple cold front edges and boxy wings are consistent with those expected to be formed by Kelvin–Helmholtz instabilities and gas sloshing in inviscid gas. The arc-shaped slingshot tail morphologies seen in each galaxy suggest that the dominant galaxies are near their orbital apogee after having experienced at least one core passage at a large impact parameter.

Unified Astronomy Thesaurus concepts: Galaxy environments (2029); Galaxy mergers (608); Cool intergalactic medium (303); X-ray astronomy (1810); Galaxy groups (597)

1. Introduction

Galaxy groups and clusters grow through the merger of smaller systems. X-ray observations that measure the temperature, density, and entropy of the hot gas in merging galaxy groups and clusters show a wide range of complex and varied morphologies. Among these are X-ray surface brightness discontinuities (cold fronts or shocks), sweeping spiral features caused by bulk motions of the gas relative to the disturbed dark matter gravitational potential (sloshing), extended, sometimes arching tails, either stripped or partially stripped from the merging systems, and boxy, scalloped, or filamentary features characteristic of hydrodynamical instabilities, such as Kelvin–Helmholtz instability (KHI). For examples of previous studies of these morphologies in galaxy group and cluster mergers, see, e.g., the review by Markevitch & Vikhlinin (2007) and references therein. Comparisons of deep Chandra X-ray observations of complex gas features in nearby mergers with high-resolution numerical simulations matched to the merging system allow us to investigate the orbital dynamics, configuration, and age of the merging partners, while also providing a powerful tool to constrain the microphysical properties (thermal conduction, magnetic field, viscosity), chemical abundance, and dynamical state of the surrounding intracluster medium (ICM; ZuHone et al. 2011; Roediger et al. 2012b, 2013; ZuHone et al. 2013; Roediger et al. 2015a, 2015b; Su et al. 2017a, 2017b; Kraft et al. 2017). Such studies give valuable insights into the role mergers play in the evolution and metallicity of the ICM. Over the past two decades, the Chandra and XMM-Newton X-ray Observatories have allowed detailed studies of the properties of hot gas in many merging galaxy clusters. These studies have focused primarily on energetic mergers in bright massive clusters, e.g., shocks and merger cold fronts in the Bullet Cluster (1E0657-56) (Markevitch et al. 2002b), A521 (Bourdin et al. 2013), and A665 (Dasadia et al. 2016), long sloshing spirals in A2029 (Paterno-Mahler et al. 2013), and both shocks and sloshing features in the subcluster merger in RXJ 1347.5-1145 (Johnson et al. 2012; Kreisch et al. 2016) and A115 (Forman et al. 2010; Botteon et al. 2016; Hallman et al. 2018). Most deep Chandra and XMM-Newton X-ray observations of galaxy-group-scale mergers focus on minor mergers, i.e., the accretion and gas stripping of the galaxy or galaxy group as it infalls through the hot gas atmosphere of a more massive cluster. When compared to numerical simulations, these studies investigate the physics of gas stripping (ram pressure, KHI, turbulence, sloshing) and its impact on gas temperatures and gas mixing in the group. See, for example, NGC 1404 in Fornax (Machacek et al. 2005; Scharf et al. 2005; Su et al. 2017a, 2017b; Sheardown et al. 2018), NGC 4552 (Machacek et al. 2006; Roediger et al. 2015a, 2015b; Kraft et al. 2017), NGC 4472 (Kraft et al. 2011; Sheardown et al. 2019), M86 (Randall et al. 2008), and M60 (Wood et al. 2017; Sheardown et al. 2019), all in the Virgo cluster, LEDA in Hydra A (De Grandi et al. 2016; Sheardown et al. 2019), and the G3–G5 group in A2142 (Eckert et al. 2017). However, these examples do not probe the earliest stages of structure formation, when low-mass groups first begin to merge.

Compared to clusters, mergers within and between galaxy groups are more difficult to study because of their lower X-ray luminosities. Previous studies have focused on the identification of sloshing features in the dominant group galaxy caused by a recent off-axis encounter with another galaxy in the group, such as in NGC 5846 (Machacek et al. 2011), NGC 5044 (David et al. 2009; Gastaldello et al. 2009; O'Sullivan et al. 2014), and IC 1860 (Gastaldello et al. 2013). Mergers between galaxy groups of equal or comparable size (major mergers) are not as well studied. Note, however, the disturbed X-ray morphologies found in the merging NGC 6868 and NGC 6861 groups (Machacek et al. 2010), the merging cold fronts in the NGC 7619 and NGC 7626 groups in Pegasus (Randall et al. 2009), and the more recent deep Chandra observations of

extremely violent (Mach >2) galaxy group mergers concurrent with active galactic nuclei (AGN) activity in RXJ0751.3+5012 (Russell et al. 2014) and NGC 6338 (O'Sullivan et al. 2019).

In this paper, we discuss the interaction of the NGC 7618 and UGC 12491 galaxy groups. At a luminosity distance of 75 Mpc, angular separation of only 14.′1, and radial velocity difference $\delta v_r = 17$ km s^{-1} (Huchra et al. 1999), NGC 7618 and UGC 12491 might appear to be natural candidates for an interacting system. However, due to their low Galactic latitudes ($\sim -17°$) and apparently undisturbed stellar morphologies (see the lower panel of Figure 1), early optical and infrared studies of these nearby elliptical galaxies misidentified them as isolated galaxies (Colbert et al. 2001). NGC 7618 hosts an ultra-steep spectrum radio source (γ(325 MHz–1.4 GHz) = −1.42) at its optical center, suggesting the presence of an AGN (De Breuck et al. 2000). This is further evidenced by the ROSAT observation of a bright X-ray point source (1RXSJ231947.4 +4) coincident with NGC 7618's center (Voges et al. 1999). UGC 12491 also hosts a weak, compact radio source at its optical center consistent with an AGN (Condon et al. 2002). However, extended radio structures have not been observed in either galaxy.

Using X-ray observations of NGC 7618 and UGC 12491 taken with the Advanced Satellite for Cosmology and Astrophysics Gas Imaging Spectrometer (ASCA GIS), Kraft et al. (2006) found highly asymmetric, ∼1 keV X-ray emission extending to radii of 150–200 kpc from each galaxy, far greater than expected for the hot gas halo of an elliptical galaxy alone. The hot gas temperatures and total X-ray luminosities around each galaxy were more typical of that expected for poor galaxy clusters or fossil groups. In their analysis of the ASCA GIS images, Kraft et al. (2006) also found that the galaxy groups were embedded in faint, diffuse gas with a temperature of ∼2 keV, albeit with large uncertainties, suggesting that the groups may be bound within a more massive dark matter halo. From a 1999 December 10 Chandra observation of NGC 7618 (ObsId 802) with a useful exposure of ∼8.4 ks, Kraft et al. (2006) identified a sharp surface brightness discontinuity to the north and a faint tail to the south of NGC 7618. They concluded that the observed features were merger induced, either through the major merger of two roughly equal-mass galaxy groups or through the infall of each group into a more massive dark matter potential. This merging hypothesis was strengthened by Crook et al. (2007, 2008), who used a variable-linking-length percolation group finding algorithm (Huchra & Geller 1982) on galaxy data from the Two Micron All Sky Survey Redshift Survey (Huchra et al. 2012) to search for nearby galaxy groups down to low Galactic latitudes. They found NGC 7618, UGC 12491, and eight additional galaxies to be members of a galaxy group (HCD 1239) with group virial mass, virial radius, and line-of-sight (LOS) velocity dispersion of $3.96 \times 10^{13} M_{\odot}$, 1.1 Mpc, and 181.7 km s^{-1}, respectively. However, due to the low galaxy number density, they could not identify substructure within the HCD 1239 group.

In 2007 NGC 7618 and UGC 12491 were each observed again with Chandra ACIS-S for effective exposures of 33 and 31.7 ks, respectively. The analysis of the X-ray data by Roediger et al. (2012a) confirmed the hypothesis of an off-axis merger of two roughly equal-mass galaxy groups. They found the hot gas in and around each galaxy to be highly disturbed, with arc-like cold fronts, long curved tails, and wings and boxy features suggestive of KHI, consistent with features found in numerical simulations of more massive galaxy cluster mergers (ZuHone et al. 2010; Roediger et al. 2012b). The disturbed X-ray gas morphologies, observed in each galaxy group by Roediger et al. (2012a) and studied in more detail in this work (e.g., see Figure 1), can be used to probe the tidal and gas hydrodynamical forces at work in the merger without the added complication of strong AGN feedback. This makes the merger of NGC 7618/UGC 12491 an ideal laboratory to measure the properties of merger-induced hydrodynamical instabilities, such as KHI. Thus, the NGC 7618/UGC 12491 merger is one of the best examples of a major merger of two, cool (∼1 keV) equal-mass galaxy groups in the local universe.

Based on the small radial velocity difference and well-defined cold fronts, previous work interpreted the merger of NGC 7618 and UGC 12491 to be occurring in the plane of the sky (Kraft et al. 2006; Roediger et al. 2012a, 2012b). However, recent simulations suggest an alternative hypothesis, in particular, that the dominant group galaxies are near the apogee of their orbits, with a viewing angle for the merger ∼45° to the LOS (Sheardown et al. 2019). At apogee, the groups would have little motion relative to each other. Thus, an observation along any LOS would produce an almost zero radial velocity difference. The inclination of the merger plane would, however, impact other characteristics, e.g., how tightly wound the spiral tails appear.

In this work, we combine the archival Chandra observations reported above with more recent Chandra observations for total useful exposures of 50.4 ks for NGC 7618 and 147 ks (98.7 ks) for imaging (spectral) analyses of UGC 12491, respectively. In Figure 1 we show the mosaic of background-subtracted, exposure-corrected, co-added 0.5–2 keV images of NGC 7618 and UGC 12491, binned by 8 Chandra pixels, to capture both merging galaxy groups and highlight faint X-ray features. Point sources, other than the galaxies' central AGNs, have been excluded to focus on the properties of the diffuse gas. The richness and complexity of the observed gas features within and around each dominant group galaxy are stunning. Using imaging and spectral analyses of these data, we show that the measured density and temperature structure of the observed hot gas strongly suggest the latter interpretation is correct.

This paper is organized as follows: In Section 2, we describe the data reduction and cleaning of the Chandra observations used in our analysis. In Section 3, we use background-subtracted, exposure-corrected, co-added images of the merger to identify the X-ray gas morphologies in and around each dominant galaxy. For each galaxy, we characterize these features using simple gas density models to fit the observed X-ray surface brightness profiles across the regions of interest, and measure the corresponding temperatures and metal abundances of the hot gas in the galaxies and in the surrounding intra-group gas (IGM). In Section 4, we compare our results to the gas morphologies found in simulations of equal-mass mergers and expected from models of gas stripping via KHI to determine the stage of the merger and microphysical properties of the galaxy and intra-group gas. We summarize our results in Section 5. All coordinates are J2000. Assuming a Hubble constant of $H_0 = 69$ km s^{-1} Mpc^{-1} in a flat Lambda cold dark matter cosmology ($\Omega_m = 0.3$), and the luminosity distance to NGC 7618 of 75 Mpc, $1'' = 0.36$ kpc (Wright 2006).

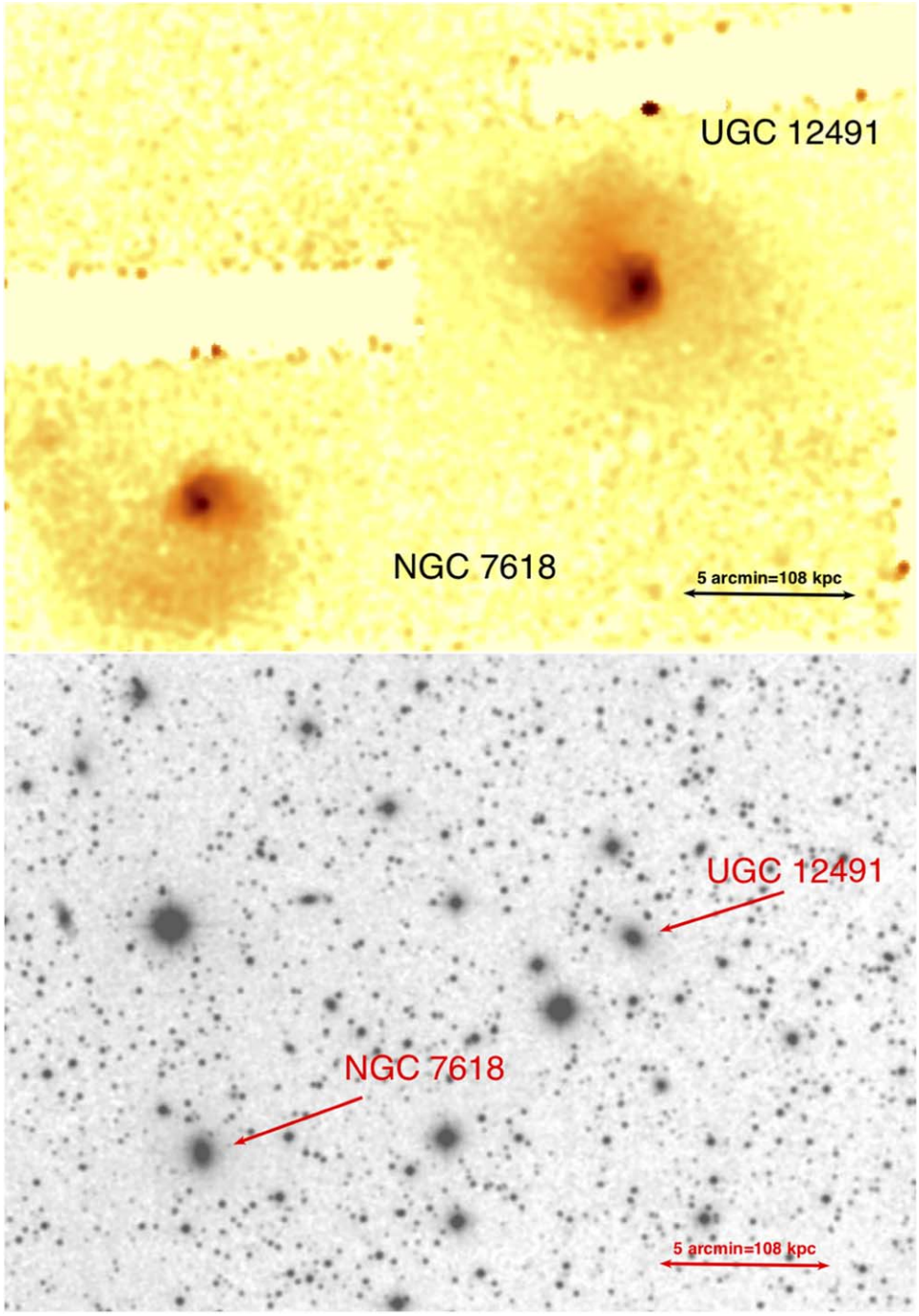

Figure 1. (Upper panel) Exposure-corrected, background-subtracted, co-added Chandra X-ray image in the 0.5–2.0 keV energy band of the hot gas associated with the NGC 7618 (lower-left panel) and the UGC 12491 (upper-right panel) galaxy groups. Point sources have been excluded. The data have been binned by 8 × 8 Chandra pixels, such that in the image 1 pixel = $3\farcs936 \times 3\farcs936$, and smoothed with a 3σ Gaussian kernel to highlight the faint emission in the tails. North is up and east is to the left. (Lower panel) DSS optical image of NGC 7618 (lower-left galaxy) and UGC 12491 (upper-right galaxy) matched to the Chandra X-ray image in WCS coordinates.

2. Observations and Data Reduction

In Table 1 we list the Chandra observations used in this analysis. All of the observations use the Advanced CCD Imaging Spectrometer array (ACIS) in VFAINT mode with the back-illuminated chip S3 at the aimpoint. Three observations (ObsIDs 7896, 16015, and 17412) place UGC 12491 near the aimpoint on chip S3, while two observations (ObsIDs 7985 and 16014) place NGC 7618 at the aimpoint.

Since source emission fills the S3 CCD for each observation, we cannot use local background subtraction for our data. Instead, we use source-free (blank-sky) background data sets available in the CIAO Calibration Data Base (CALDB) appropriate for the ACIS CCD and date of observation. However, these blank-sky data sets were taken at high Galactic latitude, while the NGC 7618 and UGC 12491 galaxy groups are at relatively low ($\sim -17°$) Galactic latitude such that additional backgrounds not accounted for in the standard blank

sky background subtraction procedure may be a concern. To investigate this possibility, we also analyze X-ray emission on the ACIS CCD S1 for ObsIDs 17412 and 16015. ACIS CCD S1 is also back-illuminated and was on in our observations. For our observations, the orientation of the ACIS detector places the center of the S1 CCD $\sim 16'$ west of the S3 aimpoint. For observations with NGC 7618 at the S3 aimpoint, this is in the direction of UGC 12491, and as can be seen in Figure 1, positions S1 near (in projection) UGC 12491 where IGM X-ray emission from the merging system is expected to be significant. This makes the S1 data in these observations unsuitable for the study of additional backgrounds. In contrast, for ObsIDs 17412 and 16015 with UGC 12491 at their respective aimpoints, the center of the S1 CCD lies (in projection) $\sim 16'$ west of UGC 12491 in a direction away from NGC 7618, where the contribution to the X-ray emission from the hot gas halo in the merger is expected to be small.

All data were reprocessed using standard CIAO 4.9 tools to apply the most current calibrations and instrument corrections, including corrections for the charge transfer inefficiency on the ACIS CCDs, the time-dependent build-up of contaminant on the optical filter, and the secular drift of the average pulse-height amplitude for photons of fixed energy (tgain). In addition to the standard rejection of events with bad array patterns (grades 1, 5, and 7), events flagged by VFAINT mode as having excess counts in border pixels were also excluded in order to maximize signal-to-noise at energies below 2 keV, where most of the source emission is observed.

After point sources were excluded, the data were cleaned using the 2.5–7 keV energy band on CCD S3 and the 2.5–6 keV energy band on CCD S1 to be consistent with the cleaning algorithm used for blank-sky backgrounds for the S3 and S1 CCDs, respectively, and date of observation. Light curves were extracted for each observation to identify large flares. For observations 7895, 7896, 16015, and 17412, periods of anomalously high and low count rates were excluded using CIAO tools *deflare* and *lc_clean* to compute the mean count rate using a 3σ algorithm and then excise time periods where the observed count rate deviated by more than 20% from that mean. Observation 16014 was contaminated by a class X1.6 solar coronal mass ejection (CME) 20 ks after the start of the observation. Examination of the light curve showed significant post-flare *ringing* of the CCD throughout the rest of the observation, such that we excluded all post-flare data from that observation. This resulted in an effective exposure for ObsID 16014 of 17.4 ks. Although the light curve for ObsID 16015, taken 7 days prior to the major solar CME, showed no obvious flaring, the mean cleaned count rate was 77% higher than the mean cleaned count rate for ObsID 17412 taken 10 days later with the same aimpoint. Such a rapid and large change in the mean count rate after standard cleaning is symptomatic of low-level flare contamination throughout ObsID 16015.

We used the CIAO tool *blanksky* to construct background files for imaging and spectral analysis from the source-free (blank-sky) background data sets available in the CIAO Calibration Data Base (CALDB) appropriate for the ACIS CCD and date of observation, and reproject them onto the observation. Identical cleaning was applied to both the blank-sky background and source data. The normalization of the blank-sky background to each source observation was fine-tuned by matching the blank-sky background count rates to the respective source count rates in the 9–12 keV energy band, where particle backgrounds dominate.

Table 1
Chandra Observations of UGC 12491 and NGC 7618

ObsID	Date	Exposure (s)	Cleaned Exposure (s)
UGC 12491			
7896	2007 Sep 3	33,613	31,728
17412	2014 Sep 13	68,005	66,978
16015	2014 Sep 3	48,425	48,422
NGC 7618			
7895	2007 Sep 8	34,059	33,033
16014	2014 Sep 10	119,424	17,401

Note. ObsID 16015 is excluded from the spectral analyses of the UGC 12491 group due to low-level flare contamination that could not be isolated and removed from the data using standard techniques.

Ciao tool *blanksky_image* was used to create source, blank sky, and blank-sky-subtracted images for the S1 data in the flare-free data set ObsId 17412 and the flared data set ObsId 16015. After excluding point sources, we use the ObsId 17412 S1 source, blank-sky background, and background-subtracted images in the 0.5–2 keV band of interest to study the importance of any residual background. We find excess emission in the 0.5–2 keV band is small ($\sim$15%) relative to the blank-sky background and is uniform over the chip. This should have a negligible effect on the results of our analysis.

We then use the 0.5–2 keV blank-sky-subtracted image of the S1 chip for ObsId 16015 to study the spatial distribution of the low-level flare in this observation. We find that the excess emission shows no significant structure across the chip. Since this background due to soft (low-level) flaring is found to be uniform across the ACIS back-illuminated CCDs in ObsId 16015, it will not distort the imaging results for the sloshing and hydrodynamic-instability-induced features of interest in this study. We thus include it in our imaging analysis. However, the spectral shape of such low-level flaring is different from that of the blank-sky backgrounds, so it cannot be eliminated from the spectral analysis by a simple renormalization of the blank-sky backgrounds at high energies. The spectral properties of such soft flares adversely affect measurements of the spectral properties of interest for the diffuse gas in the merging galaxies. APEC model fits to the solar flare contaminated data in ObsID 16015 yield anomalously high temperatures, inconsistent with the gas temperature measured from APEC model spectral fits to the other observations (ObsID 7896 and ObsID 17412) of UGC 12491. Note that Markevitch (2002a) found a similar anomalous increase in the fitted gas temperatures in Chandra observations of A1835, taken using the ACIS back-illuminated CCD S3, due to contamination by soft flares. Thus, we do not use data from ObsID 16015 in our spectral analysis of UGC 12491.

After cleaning, we found the combined effective exposure for the NGC 7618 group to be 50,434 s. The combined useful exposure for the UGC 12491 group is 147,128 s for imaging and 98,706 s for spectral analyses (see Table 1). Background-subtracted source images from CCD S3 for each observation, constructed using the CIAO tool *blanksky_image*, were co-added and exposure corrected to create mosaics for use in our imaging analysis. Point sources were excluded from these

mosaics to focus on the properties of the X-ray emission from the diffuse hot gas.

Spectra for the regions of interest were extracted for identical source and blank-sky background regions for each flare-cleaned observation using the CIAO tool *specextract*. All resolved point sources, including the central AGN for each galaxy, were excluded from these spectral regions. The background-subtracted spectra for each region were fit jointly using the HEASOFT spectral fitting package XSpec 12.10.0e (Arnaud 1996) with solar abundance tables from Anders & Grevesse (1989). Unless otherwise indicated, quoted uncertainties are 90% CL.

3. Anatomy of a Merger: KHI Wings, Sloshing Edges, and Tails

In Sections 3.1 and 3.2, we use high-resolution 0.5–2 keV Chandra X-ray images of UGC 12491 and NGC 7618, the dominant galaxy in each group, to characterize the gas morphology in and around these galaxies. For each dominant group galaxy, we use X-ray surface brightness profiles to identify surface brightness discontinuities (edges) and to study their tails. We parameterize the gas morphology by integrating simple gas density models along the LOS to reproduce the observed surface brightness profiles. We measure the hot gas temperatures and abundances along these profiles, in the X-ray detected wings, tails, and surrounding IGM, and calculate effective gas density, temperature, and pressure ratios across the X-ray surface brightness edges.

3.1. UGC 12491

In the upper panel of Figure 2, we present the high-resolution 0.5–2 keV background-subtracted, exposure-corrected co-added Chandra X-ray image of UGC 12491 with a total effective exposure of 147 ks. The image has been binned by two instrument pixels such that $1\,\mathrm{bin} = 0\farcs984 \times 0\farcs984$ and smoothed with a $1''$ Gaussian kernel. The peak X-ray surface brightness is coincident with the optical center of the galaxy. However, the observed diffuse X-ray gas distribution about the galaxy's center is highly asymmetric. To the west, there is a bright, elliptical leading edge that for simplicity we label as "Nose". The center of the ellipse that traces the Nose is displaced 6.8 kpc to the southeast of the optical center. This displacement of the brighter (denser) galaxy gas to the south of the galaxy's center is consistent with merger-induced sloshing. The leading edge is not smooth, but appears ragged or scalloped on scales of $\sim 6''$–$10''$ ($\sim$2–3 kpc).

An apparently bifurcated X-ray tail emerges from UGC 12491 toward the east and northeast. The southern segment of the tail extends $\sim$60 kpc to the east before either fading into the surrounding IGM, or joining the northern tail segment that, in projection, forms a tightly wound spiral to the north and west around the galaxy. Excess emission, measured relative to that from the IGM to the southeast away from the tail, is observed directly to the west (in front) of the Nose. This excess emission appears to connect smoothly to the westward arc of the tail and so may be a continuation of its westward spiral (see also Figure 1).

There are two wing features (Figure 2 top panel). The South Wing appears in projection arc-like with its wing *tip* extending just south of the southern tail segment. The North Wing is boxy, with two bright surface brightness edges. The innermost edge of the North Wing follows an extension of the ellipse that traces the Nose edge. The second bright edge may separate disturbed galaxy gas, possibly in the process of being stripped by KHIs, from gas in the tightly wound tail, seen in projection. In the lower panel of Figure 2, we superpose regions on the X-ray image of UGC 12491, which we use in the following subsections to construct and parameterize surface brightness profiles across edges and along part of the tail and to measure hot gas temperatures and abundances in these regions of interest.

3.1.1. X-Ray Surface Brightness Profiles

To characterize the complex gas morphologies observed in UGC 12491, we construct X-ray surface brightness profiles from the background-subtracted, exposure-corrected, co-added 0.5–2 keV image shown in Figure 2. We identify sectors containing one or more surface brightness discontinuities (*edges*) and define for each sector of interest a bounding ellipse that traces the morphology of a dominant edge-like feature in that sector (see the lower panel of Figure 2 and Table 2). The complete definition of each bounding ellipse used in our analysis of UGC 12491 is given in Appendix B. The surface brightness profile within each sector is then constructed by measuring the 0.5–2 keV X-ray surface brightness in elliptical annuli concentric to the bounding ellipse, using increasing logarithmic radial steps to move across the edges from small to large radii.

We use four sectors to study the gas features of interest in UGC 12491. We use a profile to the west across the sharp Nose feature to probe the gas properties within and outside the leading edge, and a profile predominantly to the north to study the hot gas properties across multiple edges in the boxy North Wing feature ("North Wing"). We use a profile to the east ("Inner Tail E") centered on UGC 12491's X-ray peak to study the properties of hot gas as one moves from the central region of the core to the inner edge of the tail before the tail appears, in projection, to bifurcate and curve to the north and west. For comparison, we use a similar sector to the west ("Inner W") also centered on the galaxy's X-ray peak. The resulting surface brightness profiles, shown in Figure 3, confirm the complex, multiple edge-like gas features visible in the images.

We fit the surface brightness profiles in Figure 3 by integrating simple power-law gas density models along the LOS with a *jump* in the density at each surface brightness discontinuity (edge), using a multivariate χ^2 minimization algorithm developed by M. Markevitch (private communication). We fit across multiple edges iteratively, first fitting for the location and jump of the outermost edge allowing the edge location, jump, and outer and inner power-law indices to vary. We then move inward, fixing the location of the outer edge and the power-law index outside that edge, but allowing the outer edge jump, the next inner edge location, and its jump, as well as the power-law indices on each side of the next inner edge, to vary. We proceed similarly for additional edges, as we move to smaller radii. A detailed description of the density models and of the fitting procedure used to model the profiles with multiple edges in Figure 3 is given in Appendix A. Within and near the galaxy, these spherically symmetric models may be a reasonable approximation to the hot gas density. However, at large radii, spherical symmetry may no longer hold, as one looks through tail gas that is either fully or partially stripped. These models should then be interpreted as descriptive, providing a

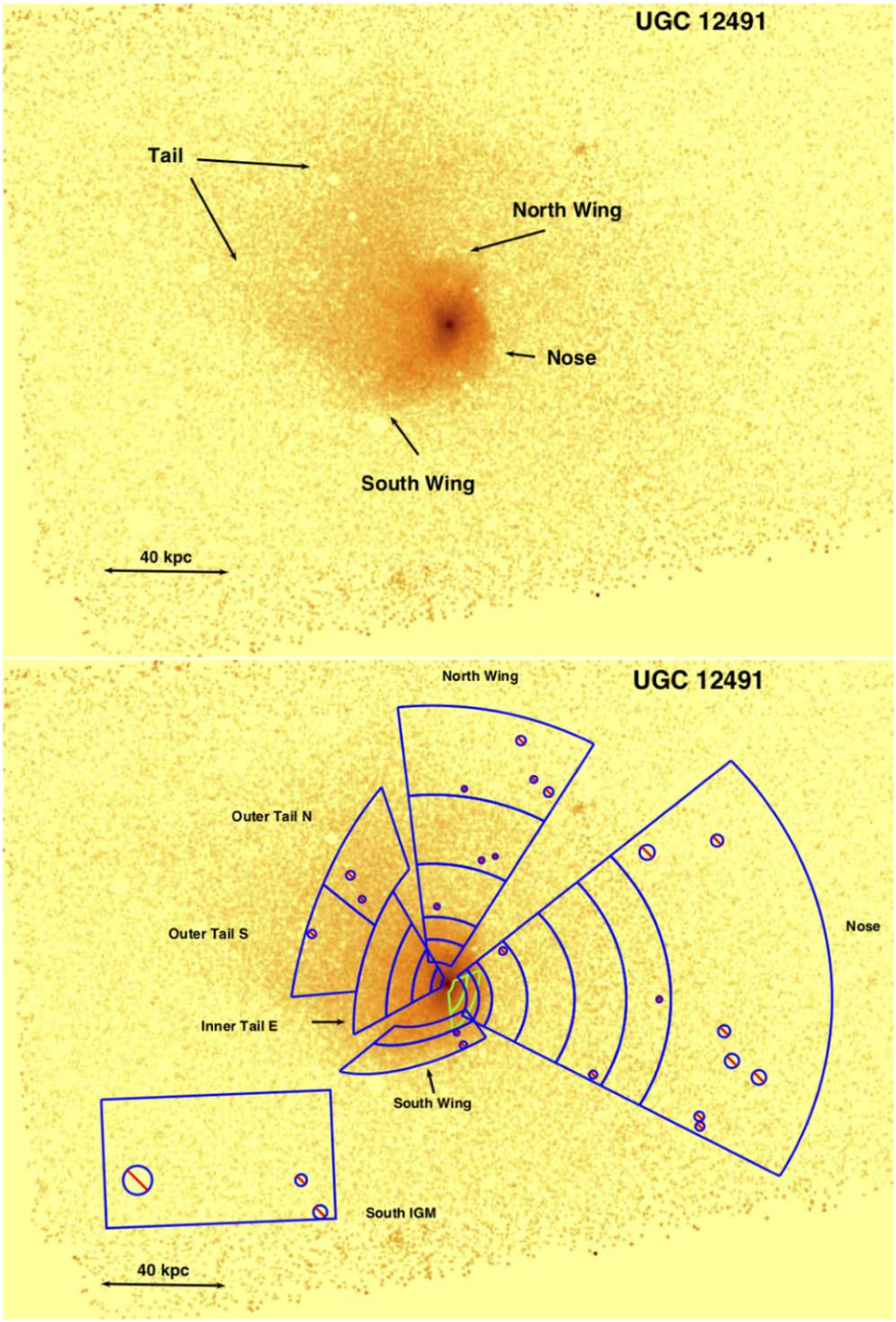

Figure 2. (Upper panel) 0.5–2 keV background-subtracted, exposure-corrected co-added Chandra X-ray image of UGC 12491 with a combined useful exposure of 147 ks. Point sources other than the central AGN have been excluded and the image is smoothed by a 1″ Gaussian kernel. 1 pixel = 0.″984 × 0.″984. North is up, west is to the right, and 40 kpc = 1.′85. (Lower panel) Sectors for the X-ray surface brightness profile analysis from Table 2 and the spectral regions defined in Appendix B are overlaid on the Chandra image of UGC 12491. The Inner W regions, chosen for comparison with the Inner Tail E regions, are shown in green. The box spectral region (South IGM) is chosen in the direction of NGC 7618 to measure the gas properties of the IGM between the merging groups. The resulting surface brightness profiles are shown in Figure 3.

simple parameterization that can be used to quantitatively compare the observational data with simulations.

The best density model fits to the surface brightness profiles are overlaid on the data in Figure 3. Table 3 lists the best-fit density power-law indices. Table 4 gives the edge locations and jumps. All given uncertainties are 90% CL. For two profiles, Inner Tail E and Inner W, the uncertainty in one or more variables is poorly determined. The shape of the single-edge model does not provide a good description of the Inner Tail E profile. While the multiple-edge model does describe the Inner Tail E surface brightness profile well, the locations of the two outer edges in the multi-edge model are not well determined because the fitted jumps for those edges are close to 1. Thus, the shape of the profile across the two outer edges of the Inner

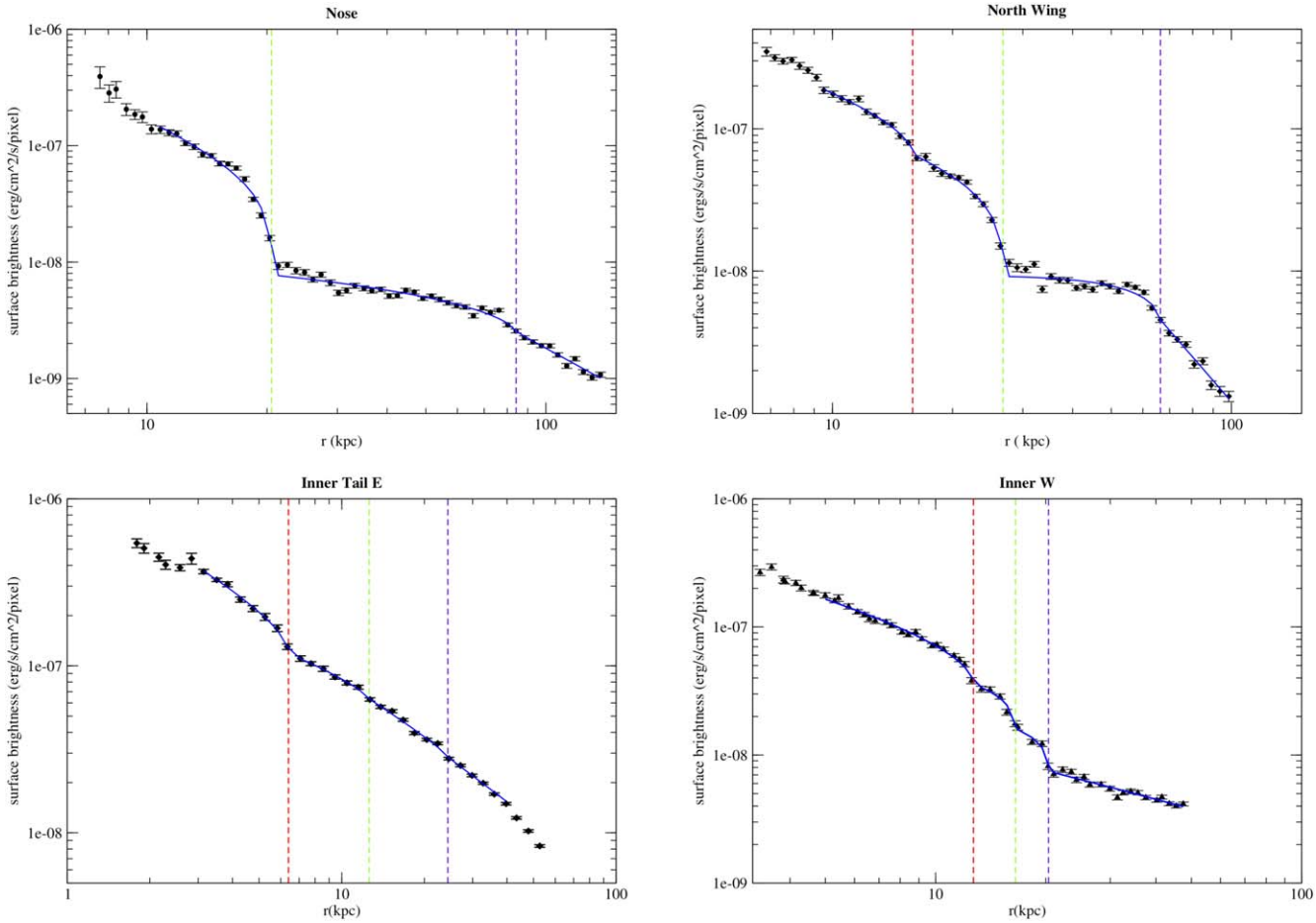

Figure 3. 0.5–2 keV X-ray surface brightness profiles of UGC 12491 constrained to sectors shown in the lower panel of Figure 2 and listed in Table 2. Each profile is superposed with the power-law density model fits (solid line) listed in Tables 3 and 4. Vertical dashed lines denote the location of edges. From top left to bottom right, the profile regions are the Nose with edges at 20.52 kpc (green) and 84.2 kpc (magenta); North Wing with edges at 15.9 kpc (red), 26.8 kpc (green), and 66.4 kpc (magenta); Inner Tail E with edges at 6.4 kpc (red), 12.6 kpc (green), and 24.4 kpc (magenta); and Inner W with edges at 12.7 kpc (red), 16.5 kpc (green), and 20.3 kpc (magenta).

Table 2
UGC 12491 Profile Sectors

Profile Label	A (deg)	B (deg)
Nose	333	38.2
North Wing	57.2	96.75
Inner Tail E	120.4	208.5
Inner W	276	22.4

Note. Each sector is centered at the center of the bounding ellipse for the corresponding region. See Appendix B for complete definitions of the bounding ellipses for these regions. Each sector subtends the angle from angle A to angle B, with all angles measured counterclockwise from the west.

Table 3
UGC 12491 Density Model Power-law Indices

Profile Label	α_1	α_2	α_3	α_4
Nose	$-1.19^{+0.15}_{-0.09}$	$-0.47^{+0.05}_{-0.06}$	$-1.44^{+0.09}_{-0.09}$	…
North Wing	$-0.86^{+0.22}_{-0.22}$	$-0.83^{+0.15}_{-0.13}$	$0.10^{+0.13}_{-0.06}$	$-2.12^{+0.12}_{-0.12}$
Inner Tail E	$-0.92^{+0.12}_{-0.15}$	$-0.67^{+0.21}_{-0.06}$	$-0.97^{+0.15}_{-0.07}$	$-1.12^{+0.01}_{-0.10}$
Inner W[a]	−0.83	−0.14	−0.055	−0.84

Note. Density model power-law indices α labeled by increasing integers from inside the innermost edge to outside the outermost edge. Superscript *a* indicates the uncertainty analysis failed to converge due to too few data points between the edges. All other quoted uncertainties are 90% CL.

Tail E region behaves more like a broken power law than the characteristic shape expected for a contact discontinuity. For the Inner W profile, the uncertainties in the model parameters are difficult to measure because there are too few radial bins ($\leqslant$4) between the edges for the error analysis to converge. However, the data do not support decreasing the profile step size further in an attempt to better define the profile between these edges because of the increase in scatter in the measured surface brightness when measured in these smaller bins.

We note that the model jumps listed in Table 4 are only proportional to the ratio of the hot gas density inside the edge to that outside the edge, with a proportionality constant given by $\sqrt{\Lambda_o/\Lambda_i}$ where Λ_o (Λ_i) is the X-ray cooling function for gas outside (inside) the edge (see, for example, Machacek et al. 2005, 2006). As discussed by Vikhlinin et al. (2001), for massive X-ray clusters where the gas temperature is much greater than 2 keV, gas cooling is dominated by the continuum emission, such that the X-ray cooling functions are only weakly dependent on gas temperatures and abundances. Thus, for massive clusters, the ratio of the cooling functions on either side of the edge is $\sim$1, and the fitted edge jump in these models is equal to the ratio of the hot gas density across the edge.

However, for low-mass galaxy groups with gas temperatures ~1 keV, as is the case for the UGC 12491 and NGC 7618 galaxy groups, line cooling dominates and the cooling functions are very sensitive to the metal abundances in the gas. Since the metal abundances can vary significantly between galaxy gas and the IGM, the ratio of cooling functions cannot be ignored. We thus refer to the density model fit parameters j_{ek} in Table 4 simply as jumps and defer the determination of the corresponding gas density ratios until after the discussion of the spectral properties of the hot gas along the profiles and in other features of interest.

3.1.2. Spectral Analysis

We fit the X-ray spectra extracted from the regions shown in the lower panel of Figure 2 using an absorbed APEC model (Smith et al. 2000) for thermal emission from an optically thin, collisionally ionized plasma with fixed Galactic hydrogen column density $n\mathrm{H} = 1.18 \times 10^{21}\,\mathrm{cm}^{-3}$ (Dickey & Lockman 1990) and photoionization absorption cross sections taken from Verner et al. (1996). We note that Kraft et al. (2006) determined from ACIS GIS observations that the X-ray emission from hot gas in this merger extends well beyond the optical disks of the dominant group galaxies, and as also shown in Figure 1, the emission does not follow the optical light. For such gas-rich low-mass galaxy groups dominated by emission ~1–2 keV, the contribution to the X-ray emission from unresolved stellar sources such as low-mass X-ray binaries can be neglected (Revnivtsev et al. 2008).

Our results are given in Table 5. The temperatures of hot gas within UGC 12491 (see the Nose1, Nose2, North Wing1,2, and S Wing1 regions, both the Inner W and Inner E Tail1,2 regions) are ~1 keV with abundances of ~0.3–0.5 $Z_\odot$. The temperature of group gas to the south, measured in the South IGM region (see Table 5) is higher ($1.30^{+0.06}_{-0.09}$ keV) and the abundance lower ($0.18^{+0.10}_{-0.07}\,Z_\odot$), as one would expect for group gas gravitationally bound to its more massive dark matter halo before the group gas has become enriched.

The measured abundance is also low ($\sim 0.14^{+0.07}_{-0.60}\,Z_\odot$) for the $1.27^{+0.07}_{-0.09}$ keV gas outside the outermost edge of the North Wing in the North Wing5 region (see Table 5). For the North Wing regions between the second and third edges (North Wing3,4 regions in Table 5), the hot gas temperature is also consistent with that of the group gas to the south. However, the abundances in the North Wing3 and North Wing4 regions are modestly higher, albeit with large uncertainties, and more similar to those measured in the Outer Tail N and S regions. The highest gas temperatures and most dramatic change in temperature occur to the west, across the inner bright edge of the Nose region, where temperatures increase from $1.05^{+0.02}_{-0.03}$ keV inside the edge to 1.5–1.6 keV outside the edge. This gas temperature is higher than elsewhere in the group IGM, suggesting that the gas may have been heated either by subsonic compression or shocks at some point in the merger history. Gas temperatures along the tail to the east increase from 1.0 keV at a radial distance $r \sim 3$ kpc from the galaxy center, consistent with hot gas within the galaxy, to 1.2 keV at $r \sim 23$ kpc, consistent within uncertainties with the temperature of the group IGM measured in the South IGM and North Wing5 regions (see Table 5). Although the uncertainties are large, the metal abundances in the tail are higher than those measured away from the tail in the group IGM. This is consistent with the tail being composed of higher abundance stripped or partially stripped galaxy gas viewed through and/or being mixed with the lower abundance group IGM. The measured Fe abundances for UGC 12491 are in agreement, within uncertainties, with Suzaku measurements (Mitsuishi et al. 2014). They find abundances of 0.2–0.4 $Z_\odot$ in the central regions of UGC 12491, declining to ~0.1–0.2 $Z_\odot$ to the southwest, midway between UGC 12491 and NGC 7618.

3.1.3. Edge Analysis: Effective Gas Densities and Pressures

We use the surface brightness profile fits combined with the spectral models for the gas to determine gas density and pressure ratios across the surface brightness edges to gain insight into the physical processes responsible for the disturbed gas morphology observed in this merger. The jumps j_{ek} and edge locations r_{ek} are labeled by increasing integers k from the innermost to the outermost edge and listed in Table 4. The jumps j_{ek} are related to the ratio n_i/n_o of the electron gas densities n_i inside the edge ($r < r_{ek}$) and n_o outside the edge ($r > r_{ek}$) through the ratio of the corresponding 0.5–2 keV X-ray cooling functions Λ_i (Λ_o) for hot gas inside (outside) the edge, respectively.

$$j_{ek}^2 = \frac{\Lambda_i}{\Lambda_o}\left(\frac{n_i}{n_o}\right)^2. \quad (1)$$

The cooling function Λ is inferred from the APEC model normalization and spectral fit properties of the gas in the regions on either side of the edge using

$$\Lambda = \frac{10^{-14} F D_L^2}{N_{\mathrm{APEC}}[D_A(1+z)]^2}, \quad (2)$$

where F is the unabsorbed model flux in the 0.5–2 keV energy band, required to match that of the surface brightness profile, N_{APEC} is the APEC model normalization, z is the redshift, $D_L(D_A)$ are the luminosity (angular size) distances, respectively, and $D_L^2 \sim [D_A(1+z)]^2$ for $z << 1$. Values for N_{APEC}, F, and Λ for each spectral region are also given in Table 5.

In Table 6, we identify each edge by the profile label and edge location and calculate the corresponding electron density n_i/n_o, gas temperature T_i/T_o, and gas pressure$_{pi}/p_o = (n_iT_i)/(n_oT_o)$ ratios across each edge. For each edge in Table 6 we list the two spectral regions on either side of the edge shown in the lower panel of Figure 2 with the region number within the sector increasing with increasing radius. For all but three edges, the effective thermal pressure ratio measured across the edge is 1 within uncertainties. This is expected for edges produced by gas sloshing. The modest overpressure ($p_i/p_o = 1.40^{+0.23}_{-0.18}$) for gas at the edge 6.4 kpc east of the galaxy center may be a sign of ongoing stripping of galaxy gas into the tail.

The effective thermal pressure ratios of $2.7^{+0.2}_{-0.3}$ and $2.4^{+0.5}_{-0.4}$ across the boxy North Wing edge at $r = 26.8$ kpc and the Nose at $r = 20.5$ kpc, respectively, are more difficult to explain. In each case, the sharp decrease in surface brightness coincides with a transition from galaxy gas to a region of excess X-ray emission that, in projection, may be composed of remnant tail and group gas. The density distribution of the more dense remnant tail may not be well described by a spherically symmetric model because of the arc-shaped morphology induced as the remnant tail outruns its parent galaxy and is carried out sidewise by the conservation of angular momentum

Table 4
UGC 12491 Density Model Edges and Jumps

Profile Label	r_{e1} (kpc)	j_{e1}	r_{e2} (kpc)	j_{e2}	r_{e3} (kpc)	j_{e3}
Nose	$20.52^{+0.04}_{-0.10}$	$4.52^{+0.33}_{-0.28}$	$84.2^{+1.3}_{-4.5}$	$1.16^{+0.04}_{-0.04}$	…	…
North Wing	$15.9^{+0.04}_{-0.23}$	$1.35^{+0.11}_{-0.11}$	$26.8^{+0.05}_{-0.20}$	$3.82^{+0.11}_{-0.12}$	$66.4^{+0.7}_{-3.3}$	$1.20^{+0.06}_{-0.07}$
Inner Tail E[a]	$6.4^{+0.20}_{-0.10}$	$1.49^{+0.16}_{-0.12}$	$12.6^{+1.4}_{-2.6}$	$1.08^{+0.07}_{-0.06}$	24.4	$1.06^{+0.06}_{-0.02}$
Inner W[a]	12.69	1.4	16.52	1.63	20.34	2.11

Note. Best-fit radial position of edges r_{ek} and jumps j_{ek} labeled by increasing integers k from the innermost edge to the outermost edge. Note that for low-mass galaxy groups, the cooling function is sensitive to the metal abundance in the gas, such that the jumps j_{ek} listed here are only proportional to the effective gas density ratios. Superscript a indicates the uncertainty analysis failed to converge for one or more variables. All quoted uncertainties are 90% CL.

Table 5
UGC 12491 Spectral Models

Region	kT (keV)	A ($Z_\odot$)	$N_{\rm APEC}$ (10^{-4} cm^{-5})	Flux (10^{-13} erg s^{-1} cm^{-2})	Λ (10^{-23} ergs cm^3 s^{-1})	χ^2 dof^{-1}
(1)	(2)	(3)	(4)	(5)	(6)	(7)
Nose1	$1.02^{+0.02}_{-0.03}$	$0.50^{+0.18}_{-0.11}$	0.7841	1.0265	1.35	70.8/68
Nose2	$1.05^{+0.02}_{-0.03}$	$0.30^{+0.10}_{-0.07}$	0.8331	0.74289	0.92	68.3/54
Nose3	$1.52^{+0.13}_{-0.16}$	$0.13^{+0.09}_{-0.06}$	1.1707	0.6185	0.55	101.3/68
Nose4	$1.58^{+0.12}_{-0.15}$	$0.17^{+0.10}_{-0.07}$	1.3542	0.74826	0.57	80.3/86
Nose5	$1.56^{+0.11}_{-0.14}$	$0.20^{+0.10}_{-0.08}$	1.4863	0.85885	0.60	85.6/84
Nose6	$1.46^{+0.14}_{-0.12}$	$0.19^{+0.13}_{-0.08}$	1.3986	0.81482	0.60	77.3/68
Nose7	$1.49^{+0.11}_{-0.13}$	$0.14^{+0.07}_{-0.05}$	4.2165	2.2628	0.56	227.8/227
North Wing1	$0.97^{+0.03}_{-0.02}$	$0.37^{+0.11}_{-0.08}$	1.1925	1.2978	1.13	83.3/79
North Wing2	$1.04^{+0.02}_{-0.03}$	$0.27^{+0.08}_{-0.06}$	0.9713	0.81426	0.87	67.2/58
North Wing3	$1.30^{+0.05}_{-0.05}$	$0.21^{+0.07}_{-0.06}$	1.2446	0.79074	0.66	74.1/72
North Wing4	$1.25^{+0.03}_{-0.05}$	$0.33^{+0.10}_{-0.08}$	1.4146	1.1401	0.83	115.7/113
North Wing5	$1.27^{+0.07}_{-0.09}$	$0.14^{+0.07}_{-0.06}$	1.4805	0.82193	0.57	93.3/110
Inner W1	$1.02^{+0.02}_{-0.02}$	$0.37^{+0.09}_{-0.07}$	1.3729	1.4412	1.09	73.2/85
Inner W2	$1.03^{+0.02}_{-0.02}$	$0.40^{+0.11}_{-0.09}$	1.0118	1.1009	1.13	81.4/74
Inner Tail E1	$0.93^{+0.03}_{-0.03}$	$0.26^{+0.08}_{-0.06}$	1.2754	1.1382	0.92	75.3/66
Inner Tail E2	$1.04^{+0.02}_{-0.02}$	$0.34^{+0.08}_{-0.06}$	1.5448	1.5017	1.01	112.7/94
Inner Tail E3	$1.12^{+0.03}_{-0.04}$	$0.33^{+0.08}_{-0.07}$	2.1723	1.9398	0.92	124.7/117
Inner Tail E4	$1.21^{+0.03}_{-0.02}$	$0.55^{+0.12}_{-0.10}$	1.9291	2.1802	1.17	124.8/138
Outer Tail N	$1.16^{+0.04}_{-0.05}$	$0.31^{+0.08}_{-0.07}$	1.9460	1.626	0.87	151.2/122
Outer Tail S	$1.18^{+0.04}_{-0.04}$	$0.27^{+0.06}_{-0.05}$	2.3682	1.8089	0.79	171.2/129
South Wing1	$1.00^{+0.02}_{-0.02}$	$0.38^{+0.11}_{-0.08}$	1.2303	1.3336	1.12	77.4/84
South Wing2	$1.11^{+0.05}_{-0.04}$	$0.24^{+0.09}_{-0.05}$	1.5667	1.1929	0.79	86.4/85
South IGM	$1.30^{+0.06}_{-0.09}$	$0.18^{+0.10}_{-0.07}$	1.4386	0.87145	0.63	205/175

Note. Spectra were modeled using the absorbed APEC model (phabs ×apec) with Galactic absorption fixed at 1.18×10^{21} cm^{-3} (Dickey & Lockman 1990). All regions except the South IGM region are elliptical panda regions, shown in the lower panel of Figure 2 and defined in Appendix B. Region numbers increase from small to large radii. Columns from left to right: (1) region name, (2) temperature, (3) abundance, (4) unabsorbed X-ray flux in the 0.5–2 keV energy band, (5) APEC model normalization, (6) measured cooling function Λ in the 0.5–2 keV energy band (see Equation (2)), and (7) χ^2 dof^{-1} for the model fit.

during the galaxy's approach to apogee. A quantitative understanding of what the spherically symmetric effective fits imply about the physical three-dimensional density distribution and composition of gas in these regions requires that the same analysis be applied to mock Chandra X-ray images produced from simulation data matched to this merger. However, this is beyond the scope of the current paper.

3.2. NGC 7618

In the top panel of Figure 4, we show the 0.5–2 keV background-subtracted, exposure-corrected, mosaicked Chandra image of the NGC 7618 galaxy subgroup. Point sources, other than the nuclear point source, have been excluded. The image has 1″ pixels and has been smoothed with a 3″ Gaussian kernel to highlight the faint gas features. Asymmetric structure is observed in the hot gas in and surrounding NGC 7618, and in spite of its lower (50.48 ks) total useful exposure, the gas features in NGC 7618 are strikingly similar to those observed in UGC 12491 (shown in Figure 2). NGC 7618 has a nose-like, leading surface brightness edge to the northeast (labeled Head in Figure 4), *wings* of emission to the east and west sides of the leading edge, and a long (∼170 kpc) arced tail. At radii inside the leading edge, Figure 4 shows dense gas pushed to the northeast in a plume, before curving sharply to the north and again to the west, creating a spiral with angular (boxy) edges. This structure has been seen in previous images of NGC 7618 using Chandra ObsID 7895 (Roediger et al. 2012a; Goulding et al. 2016). The leading edge (Head) also is not smooth. A

faint, narrow (∼4 kpc wide) gas filament extends 11 kpc (∼32″) to the north, outside of the plume's boxy, spiral extension. Moving radially out from the nucleus through the West Wing region in Figure 4, we see two surface brightness edges (see also the profile analysis in Figure 5). The inner edge appears more closely associated with the Head region and inner spiral, while the outer edge could either be stripping, due to hydrodynamic instabilities, or gas from the tail seen in projection to curve around the galaxy, first to the south and then to the north.

As in Figure 2 for UGC 12491, the lower panels of Figure 4 for NGC 7618 outline the regions that are used to study the X-ray surface brightness profiles, X-ray spectra, and effective densities and pressures across the edges in Section 3.2.1, Section 3.2.2, and Section 3.2.3, respectively, superposed on the image of NGC 7618 shown in the upper panel. In the lower-left panel, we treat the Head region as a whole, using a sector with an opening angle of 93° to average over the brighter plume, and we trace the northward segment of the tail with rectangular regions. In the lower right panel, we isolate the plume using a narrower sector with an opening angle of 58°, and we also choose a sector to construct the surface brightness profile across the edge of the East Wing. Note, however, that the outer spectral region of the East Wing sector overlaps part of the Mid Tail region. The West Wing and South Tail regions are the same in each figure.

3.2.1. X-Ray Surface Brightness Profiles

To characterize the complex gas morphologies in NGC 7618, we construct X-ray surface brightness profiles from the 0.5–2 keV background-subtracted, exposure-corrected, co-added Chandra image binned by 2 × 2 instrument pixels, such that 1 bin = 0.″984 × 0.″984 (similar to that shown in Figure 4, but without Gaussian smoothing), using logarithmic radial steps constrained to lie in the sectors defined in Table 7 and shown in the lower panels of Figure 4.

Following the same procedure as in Section 3.1.1 and described in Appendix A, we fit the surface brightness profiles with a series of spherically symmetric power-law density models and jumps at each observed surface brightness discontinuity. Due to the significantly lower effective exposure for NGC 7618 caused by the solar flare contamination, fine structures within these profiles are more difficult to identify than in UGC 12491 and the fits are less robust. These X-ray surface brightness profiles, overlaid with the density model fits, are shown in Figure 5. The best-fit density model power-law indices are given in Table 8, and the edge locations and jumps are given in Table 9.

Both the West Wing and Plume profiles are best fit with multiple edges. However, the Head profile, an average over the plume and galaxy gas to the northwest of the plume inside the edge, supports only a single-edge model. The East Wing is also best fit by a single-edge model. For the South Tail, the two-edge model, shown in Figure 5, describes the data well, but the jumps are weak (∼1) such that the profile is characterized by a steepening of the power-law index from −0.72 for radii $2 < r < 7$ kpc to −1.22 for radii $7 < r < 14$ kpc to −1.37 for radii $14 < r < 30$ kpc. As also seen for the Inner E Tail of UGC 12491 in Figure 3, neither a simple power law nor a single-edge density model provides a good description of the South Tail profile, and the uncertainties in the multiple-edge model are poorly determined. We again defer the discussion of the effective gas density and pressures until after we have mapped the hot gas temperatures and abundances in and around NGC 7618.

Table 6
UGC 12491 Edge Analysis

Profile	r_e (kpc)	n_i/n_o	T_i/T_o	$_{pi}/p_o$
Nose2,3	20.52	$3.49^{+0.26}_{-0.21}$	$0.69^{+0.10}_{-0.07}$	$2.41^{+0.54}_{-0.38}$
Nose6,7	84.2	$1.20^{+0.04}_{-0.04}$	$0.98^{+0.11}_{-0.14}$	$1.18^{+0.30}_{-0.21}$
North Wing1,2	15.9	$1.19^{+0.09}_{-0.10}$	$0.93^{+0.06}_{-0.03}$	$1.11^{+0.16}_{-0.13}$
North Wing2,3	26.8	$3.33^{+0.09}_{-0.11}$	$0.80^{+0.05}_{-0.05}$	$2.66^{+0.24}_{-0.25}$
North Wing4,5	66.4	$1.00^{+0.04}_{-0.06}$	$0.98^{+0.11}_{-0.08}$	$0.98^{+0.15}_{-0.14}$
Inner Tail E1,2	6.4	$1.56^{+0.17}_{-0.08}$	$0.89^{+0.05}_{-0.04}$	$1.40^{+0.23}_{-0.18}$
Inner Tail E2,3	12.6	$1.03^{+0.06}_{-0.06}$	$0.93^{+0.05}_{-0.04}$	$0.95^{+0.12}_{-0.09}$
Inner Tail E3,4	24.4	$1.20^{+0.06}_{-0.03}$	$0.93^{+0.04}_{-0.06}$	$1.11^{+0.11}_{-0.09}$

Note. The numbers in parenthesis (i,o) following the region name indicate the spectral region inside ($r < r_e$) and outside ($r > r_e$) the corresponding edge located at radius r_e, respectively. Uncertainties for derived values assume extremes in the 90% CL uncertainties for measured properties.

3.2.2. Spectral Analysis

As in Section 3.1.2, we use an absorbed APEC model with Galactic absorption to fit the hot gas temperature and heavy element abundances in each region shown in the lower panels of Figure 4. Our results are given in Table 10 with region number increasing with increasing radius for each sector.

Spectral models for the Head1, East Wing1, West Wing1, and Plume1 regions find a hot gas temperature of 0.9 − 1 keV within the NGC 7618 galaxy, consistent with previous measurements (Goulding et al. 2016). The best-fit heavy element abundances for hot galaxy gas are $0.34^{+0.08}_{-0.06}\,Z_\odot$, $0.35^{+0.15}_{-0.10}\,Z_\odot$, $0.30^{+0.11}_{-0.08}\,Z_\odot$, and $0.45^{+0.17}_{-0.11}\,Z_\odot$ for the Head1, East Wing1, West Wing1, and Plume1 regions, respectively. These abundances are consistent with each other within their 90% CL uncertainties and are in agreement with Suzaku measurements by Mitsuishi et al. (2014). The central value for the metal abundance in the best-fit spectral model for the hot gas in the bright plume (the Plume1 region) is higher than in the other regions. Although the uncertainties are large, this may suggest that the plume is composed of higher abundance gas dredged upward from the central region of NGC 7618 either by the merger-induced tidal interactions with UGC 12491 or by sloshing.

The West Wing3 and Plume3 regions are dominated by IGM gas. Their best-fit temperatures ($1.32^{+0.14}_{-0.12}$ keV and $1.35^{+0.16}_{-0.11}$ keV) and abundances ($0.11^{+0.07}_{-0.06}\,Z_\odot$ and $0.17^{+0.13}_{-0.08}\,Z_\odot$), respectively, are consistent with the hot gas temperature and abundance measured for the IGM south of UGC 12491 in the direction of NGC 7618 (see the South IGM region in Table 5). The Head2 region contains both the IGM gas and galaxy gas in the filament and possibly KHI-induced, irregular *rolls* along the edge. The same is true of the Plume2 region. This accounts for temperatures that are intermediate between those of the IGM (see the West Wing3 and Plume3 regions) and galaxy gas (e.g., see the Plume1, Head1, and West Wing1 regions). This is also true for the East Wing2 region, which covers both IGM and tail gas.

The most interesting temperature structure is found in the tail. The gas temperature decreases with increasing radius to the south from $1.07^{+0.04}_{-0.02}$ keV in the bright innermost region to

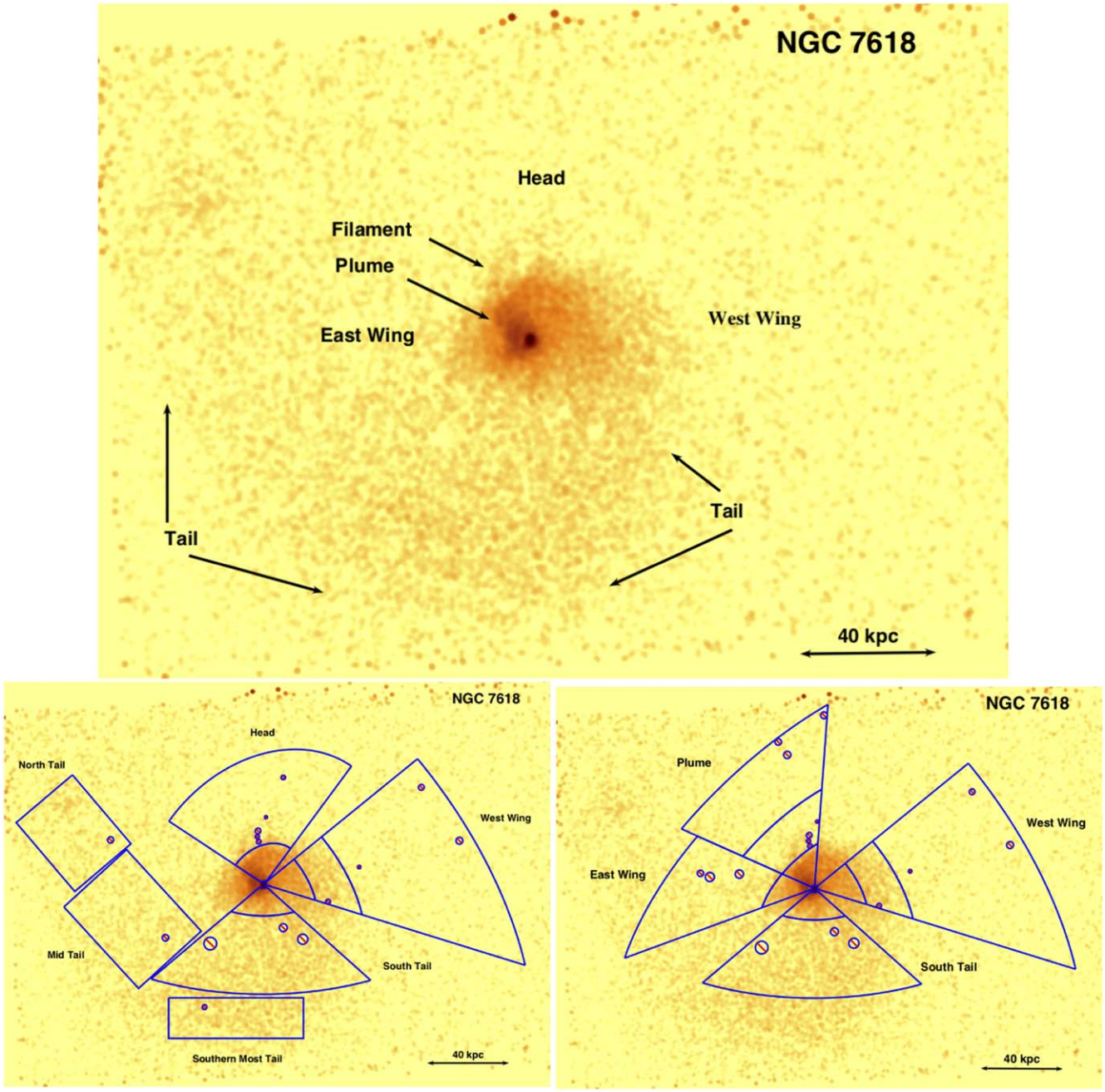

Figure 4. (Upper panel) 0.5–2 keV background-subtracted, exposure-corrected co-added Chandra X-ray image of NGC 7618 with features labeled. Point sources have been excluded and the image has been smoothed with a 3″ Gaussian kernel to highlight faint emission. 1 pixel = 0.″984 × 0.″984 and the scale 40 kpc = 1.′85. (Lower-left panel) Sectors for the X-ray surface brightness profile analysis and spectral regions emphasizing the head and tail features from Section 3.2.2 are overlaid on the Chandra image of NGC 7618 from the upper panel. (Lower-right panel) Sectors for the X-ray surface brightness profile analysis and spectral regions emphasizing the northern plume and east wing features are overlaid on the Chandra image from the upper panel.

$0.75^{+0.03}_{-0.03}$ keV in the southernmost region, before the tail is observed to turn smoothly to the north and east. Measured abundances in the same regions remain, within uncertainties, constant at ∼0.2–0.4 $Z_{\odot}$, typical of that measured for other regions within NGC 7618. Thus, both the cool gas temperatures and the heavy element abundances support the hypothesis that the observed tail is composed of galaxy gas that has been displaced, but not necessarily gravitationally unbound, from the galaxy. The temperature gradient to the south may be the result of tail gas cooling as it expands. However, it is intriguing to note that the spectral fit for the temperature and abundance for the West Wing2 region is identical to that in the South Tail2 region (see Table 10). Since these regions are at similar mean radii from the center of NGC 7618, this may suggest that West Wing2 is part of the same structure as South Tail2, forming a spiral feature that wraps continuously from the Head region into the tail, rather than an extension of West Wing1. In this latter interpretation of the tail morphology, the South Tail regions are oriented across the width of the tail rather than along its length, such that the measured temperatures reflect a temperature gradient across the width of the tail with higher temperature gas found on the inner edge of the spiral feature closest to the galaxy. Finally, as the tail turns to the north and east (the Mid Tail and North Tail regions in Figure 4 and

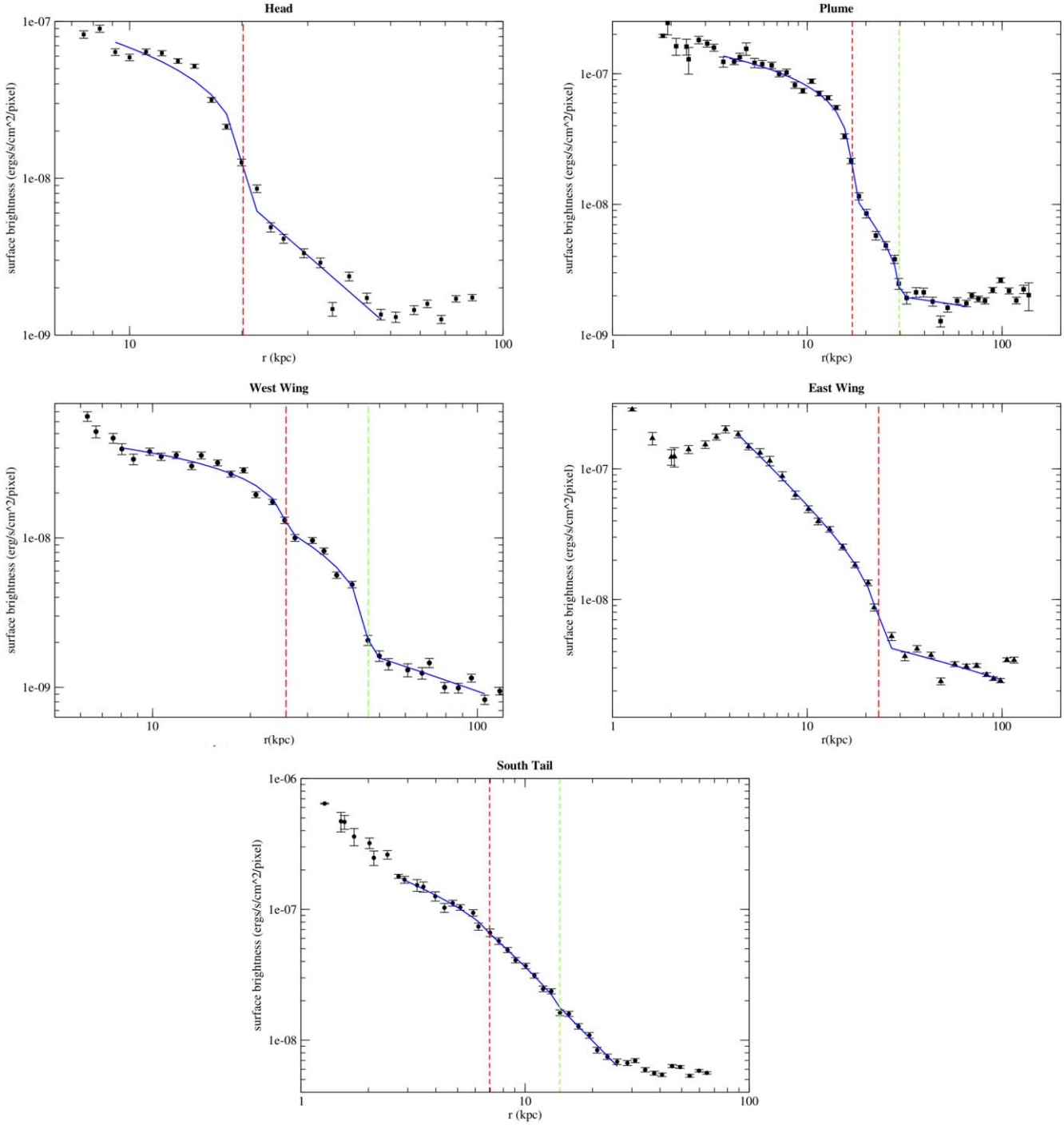

Figure 5. 0.5–2 keV X-ray surface brightness profiles of NGC 7618 labeled by and constrained to the sectors shown in the lower two panels of Figure 4 and listed in Table 7. Each profile is superposed with the corresponding power-law density model fit (solid line) listed in Tables 8 and 9. Vertical dashed lines denote the location of edges. From upper left to lower right, the profile regions are the Head with the edge at 20.15 kpc (red); Plume with edges at 17.02 kpc (red) and 29.65 kpc (green); West Wing with edges at 25.77 kpc (red) and 46.18 kpc (green); East Wing with edge at 23.27 kpc (red); and South Tail with possible weak edges at 6.95 kpc (red) and 14.3 kpc (green).

Table 10), the gas temperature slowly increases and the metal abundance decreases toward the IGM values. This is likely the result of tail gas mixing with and/or viewed through proportionately more IGM gas.

3.2.3. Edge Analysis: Effective Gas Densities and Pressures

In Table 11, we present the effective density, temperature, and pressure ratios across the edges identified in the X-ray surface brightness profiles shown in Figure 5 and listed in Table 9. For the Head and West Wing edges, the inferred effective pressure ratios are close to 1 (pressure equilibrium), as expected for merger-induced sloshing, and the shape of the profile is also typical of that expected for this model. However, the fitted density ratios (and thus the effective pressure ratio across the edge) for the outer plume edge and the eastern wing edge are unphysical (see Plume 2,3 and East Wing 1,2, respectively, in Table 11). For $r < 23$ kpc, as one moves inside

Table 7
NGC 7618 Profile Sectors

Profile Label	A (deg)	B (deg)
Head	53.4	146.4
Plume	85.7	155.8
West Wing	343.7	399
East Wing	155.9	200
South Tail	220	318

Note. All sectors are centered at the X-ray/optical peak $\alpha = 23^{h}19^{m}47^{s}22$, $\delta = +42°51'09''5$. Each sector subtends the angle measured counterclockwise from angle A to angle B. All angles are measured counterclockwise from the west.

Table 8
NGC 7618 Density Model Power-law Indices

Profile Label	α_1	α_2	α_3
Head	$-0.60^{+0.12}_{-0.08}$	$-1.54^{+0.09}_{-0.12}$	…
Plume	$-0.41^{+0.07}_{-0.05}$	$-1.44^{+0.24}_{-0.55}$	$-0.46^{+0.23}_{-0.05}$
West Wing	$-0.34^{+0.10}_{-0.09}$	$-0.83^{+0.21}_{-0.55}$	$-0.82^{+0.09}_{-0.06}$
East Wing	$-1.20^{+0.05}_{-0.04}$	$-0.63^{+0.05}_{-0.04}$	…
South Tail	−0.72	−1.22	−1.37

Note. Density model power-law indices α for the profiles shown in Figure 5. The power-law indices are labeled by increasing integers from inside the innermost edge to outside the outermost edge for each profile. All quoted uncertainties are 90% CL.

Table 9
NGC 7618 Density Model Edges and Jumps

Profile Label	r_{e1} (kpc)	j_{e1}	r_{e2} (kpc)	j_{e2}
Head	$20.15^{+0.01}_{-0.11}$	$2.42^{+0.40}_{-0.68}$	…	…
Plume	$17.02^{+0.05}_{-0.13}$	$2.37^{+0.28}_{-0.20}$	$29.65^{+0.55}_{-0.15}$	$3.27^{+0.35}_{-0.28}$
West Wing	$25.8^{+0.3}_{-2.3}$	$1.55^{+0.16}_{-0.29}$	$46.18^{+0.25}_{-0.15}$	$2.78^{+0.16}_{-0.20}$
East Wing	$23.3^{+0.07}_{-0.05}$	$3.16^{+0.39}_{-0.29}$	…	…
South Tail	6.95	1.08	14.3	1.11

Note. Best-fit radial position of edges r_{ek} and jumps j_{ek} for $k = 1, 2$ where 1, 2 label the inner and outer edges, respectively, for the profiles shown in Figure 5. All quoted uncertainties are 90% CL.

the East Wing edge, the profile may average over multiple features, such as part of the plume or an internal, sloshing spiral similar to that seen in the West Wing. Fitting a single-edge jump to multiple features would lead to an overestimate of the jump and thus an unphysical estimate for the pressure ratio across the East Wing's outer edge. The plume profile in Figure 5 clearly shows a sharp rise at $r \sim 30$ kpc merging smoothly into a steeply rising profile with decreasing radius between the outer and inner edges. The change in the surface brightness at the plume region's outer edge is a factor of 2–3, such that one would expect a physical density ratio of order 1.4–1.7 and effective pressures consistent with pressure equilibrium. However, from Figure 4 the Plume2 region between the outer and inner plume edges contains excess emission from a filament that skews the shape of the profile from that expected by the simple effective density model used in the fitting algorithm. This excess emission masks the characteristic flattening of the surface brightness profile inside the edge expected by the model.

4. Discussion and Comparison to Simulations

Simulations by Roediger et al. (2015a, 2015b) and Sheardown et al. (2019) demonstrate that the origins of the asymmetric gas features and inferred gas flow patterns, i.e., the presence of shear flows or turbulence, depend critically on the age and orbital parameters of the merger. It is essential to determine whether the observed asymmetries are produced through hydrostatic instabilities or by other means before using their properties to constrain the microphysics of the IGM. These simulations show that gas tails produced during merging activity belong to two basic classes, ram-pressure tails or slingshot tails, based on how they are formed. Thus, the morphology and spectral properties of these tails are powerful tools to distinguish the orbital age of the merger.

Ram-pressure tails are formed on the approach to perigee, as merging cores fall through IGM gas of increasing pressure. IGM gas flows around the cores are well described as flows around a blunt object, with an upstream stagnation point at the leading cold front edge, and a thermal pressure ratio between the gas pressure at the stagnation point and in the undisturbed free stream region. The ratio of these two thermal pressures can be used to infer the relative velocity between the core and the IGM (Vikhlinin et al. 2001). Strong shear flows around the core induce KHIs that create rolls, gas wings, and boxy features and also strip the outer layers of gas from the merging core to form a tail (Roediger et al. 2012a, 2015a). The ram-pressure tail consists of three parts: a *remnant tail* closest to the merging core that is composed of gas still gravitationally bound to the galaxy, a *dead water* region composed of stripped gas that has little or no velocity relative to the merging core, and a *far wake* of stripped gas flowing away (downstream) from the core and mixing with the IGM (Roediger et al. 2015a). Since mixing of the wake gas with the IGM can be strongly inhibited by IGM gas viscosity or the presence of magnetic fields, the observed length and spectral properties of ram-pressure tails place important constraints on these properties (e.g., NGC 1404 Su et al. 2017a, 2017b; NGC 4552, Kraft et al. 2017). While a ram-pressure tail is expected to point roughly opposite to the direction of infall of its merging core, the tail can be bent by bulk motions (winds) in the IGM, caused by a previous encounter of the pair, a previous merger, or AGN outbursts. Thus, the observed *ram-pressure* tail morphology is a product of the entire merger history of the system and can be complex (Eckert et al. 2017; Kraft et al. 2017).

Slingshot tails are formed as the merging cores move past each other at perigee and travel through IGM gas of decreasing pressure as the distance between the cores increases (Hallman & Markevitch 2004; Ascasibar & Markevitch 2006; Poole et al. 2006; Markevitch & Vikhlinin 2007; ZuHone et al. 2011). Simulations show that, as the cores near the apogee of their orbits, the remnant tails, composed of gas still gravitationally bound to their parent system, display complicated morphologies and temperature structures that depend strongly on the impact parameter of the merger. For large impact parameters the tails form sweeping arc-shaped structures. For small impact parameters, the tail gas overruns the parent core producing a turbulent, irregularly shaped secondary atmosphere about the parent before evolving into a cone-shaped tail pointing away from the merger partner (Sheardown et al. 2019).

Table 10
NGC 7618 Spectral Model Fits

Region	kT (keV)	A ($Z_\odot$)	Norm (10^{-4} cm^{-5})	Flux (10^{-13} erg s^{-1} cm^{-2})	Λ (10^{-23} erg cm^3 s^{-1})	χ^2/(dof)
Head1	$0.92^{+0.02}_{-0.02}$	$0.34^{+0.08}_{-0.06}$	2.91993	3.1566	1.12	141/94
Head2	$1.18^{+0.08}_{-0.12}$	$0.11^{+0.06}_{-0.04}$	2.54809	1.3649	0.55	143.8/126
Plume1[a]	$0.95^{+0.02}_{-0.03}$	$0.45^{+0.17}_{-0.11}$	2.079	2.660	1.32	50/54
Plume2	$1.06^{+0.12}_{-0.07}$	$0.12^{+0.08}_{-0.05}$	0.99045	0.5622	0.59	45.4/41
Plume3	$1.35^{+0.16}_{-0.11}$	$0.17^{+0.13}_{-0.08}$	1.3863	0.80223	0.60	104/88
West Wing1	$0.94^{+0.03}_{-0.03}$	$0.30^{+0.11}_{-0.08}$	1.58476	1.5405	1.01	72.3/59
West Wing2	$0.85^{+0.05}_{-0.04}$	$0.21^{+0.10}_{-0.06}$	1.28025	1.046	0.85	36.3/51
West Wing3	$1.32^{+0.14}_{-0.12}$	$0.11^{+0.07}_{-0.06}$	2.24625	1.1752	0.54	112.3/111
East Wing1	$0.98^{+0.03}_{-0.03}$	$0.35^{+0.15}_{-0.10}$	1.4279	1.502	1.09	45.6/55
East Wing2	$1.15^{+0.07}_{-0.08}$	$0.22^{+0.10}_{-0.07}$	1.9604	1.3908	0.73	112.3/111
South Tail1	$1.07^{+0.04}_{-0.02}$	$0.29^{+0.08}_{-0.06}$	2.03174	1.7401	0.89	80.2/70
South Tail2	$0.85^{+0.02}_{-0.02}$	$0.22^{+0.05}_{-0.04}$	4.30845	3.6458	0.88	160.5/154
Southernmost Tail	$0.75^{+0.03}_{-0.03}$	$0.25^{+0.13}_{-0.07}$	1.77932	1.6352	0.95	87.2/75
Mid Tail	$1.01^{+0.03}_{-0.04}$	$0.17^{+0.06}_{-0.04}$	2.4649	1.6566	0.70	132/112
North Tail	$1.06^{+0.08}_{-0.05}$	$0.15^{+0.06}_{-0.04}$	1.77672	1.0875	0.63	86.7/78

Note. Spectra were modeled using an absorbed APEC model with Galactic absorption fixed. Superscript *a* based on ObsID 7895 only.

In Figure 6, we show gas density, temperature, and metallicity maps, derived from a numerical simulation of the merger of two equal-mass galaxy groups at a merger age of 1.94 Gyr, as the galaxy groups approach apogee in their orbits after one previous pericenter passage (Sheardown et al. 2019). The mass of each simulated galaxy group in the merger was $6 \times 10^{13} M_\odot$. Thus, the total mass of the simulated merger is a factor 3 larger than the virial mass measured by Crook et al. (2007, 2008) for the HCD 1239 galaxy group containing NGC 7618 and UGC 12491. Initial density profiles for the groups were constructed as for the Fornax Cluster in Sheardown et al. (2018). The initial separation was taken to be 1500 kpc, twice the virial radius of each group so that initially the gas atmospheres of each merger partner do not overlap. The initial tangential velocity between the groups was chosen such that the impact parameter at the first pericenter passage (265 kpc) was large enough to produce the arc-shaped slingshot tail morphologies seen in the observation. A simulation run with smaller tangential velocity did not produce the observed well-defined arc-shaped tails, but rather resembled the overrun tail morphology discussed in Sheardown et al. (2019). The gas was assumed to have zero viscosity. The maps in Figure 6 were constructed by taking slices through the corresponding simulation data cubes at $z = 0$.

In Figures 7 and 8, we show the 90% CL intervals for the hot gas temperatures and metallicities, respectively, from the best-fit APEC spectral models listed in Tables 5 and 10 superposed on the 0.5–2 keV Chandra X-ray surface brightness images for UGC 12491 and NGC 7618 from Figures 2 and 4, respectively. Figure 6, derived from the simulations, and Figures 7 and 8, derived from the observational data, are related, but not quantitatively comparable. X-ray surface brightness, shown in the observational images, is proportional to the square of the electron density integrated along the LOS, while the simulation gas density map, constructed from a simulation slice, displays the gas density at a given LOS coordinate (here $z = 0$). Similarly, the APEC spectral model temperature and metallicity 90% CL intervals superposed on the galaxy group X-ray images in Figures 7 and 8 are projected (average) gas temperatures and metallicities for all X-ray emitting gas along the LOS, while the corresponding simulated maps in Figure 6 display a predicted gas temperature and metallicity for the specific LOS coordinate. Despite these differences, the qualitative similarities between the gas morphology and properties seen in maps derived from the numerical simulations and the related maps derived from our Chandra X-ray data, are striking.

Table 11
NGC 7618 Edge Analysis

Profile	r_e (kpc)	n_i/n_o	T_i/T_o	$_{pi}/p_o$
Head1,2	20.15	$1.70^{+0.28}_{-0.51}$	$0.78^{+0.11}_{-0.07}$	$1.33^{+0.46}_{-0.48}$
Plume1,2	17.02	$1.58^{+0.19}_{-0.13}$	$0.90^{+0.08}_{-0.12}$	$1.42^{+0.31}_{-0.29}$
Plume2,3	29.65	$3.30^{+0.36}_{-0.28}$	$0.79^{+0.16}_{-0.12}$	$2.59^{+0.89}_{-0.61}$
West Wing1,2	25.8	$1.42^{+0.15}_{-0.26}$	$1.11^{+0.09}_{-0.10}$	$1.57^{+0.31}_{-0.40}$
West Wing2,3	46.2	$2.26^{+0.13}_{-0.17}$	$0.64^{+0.11}_{-0.09}$	$1.45^{+0.32}_{-0.29}$
East Wing1,2	23.3	$2.59^{+0.32}_{-0.24}$	$0.85^{+0.09}_{-0.07}$	$2.20^{+0.45}_{-0.37}$

Note. The numbers (i, o) following the region name indicate the spectral region (inside, outside) the corresponding edge, respectively. Uncertainites for derived values assume extremes in the 90% CL uncertainties for measured properties.

4.1. Density and Surface Brightness Comparisons

Both Figures 7 and 1 show arc-shaped tails bending sharply toward and/or wrapping around the dominant merging galaxies. The arc-shaped morphology coupled with the tight winding of the tails are signatures for slingshot tails formed from the merger of two galaxy groups with a large impact parameter. Coupled with the small relative radial velocity between the two galaxies, the tail morphology strongly indicates that NCG 7618 and UGC 12491 are the dominant galaxies in two equal-mass merging galaxy groups that are near apogee in their orbits. Comparison with the simulations of Sheardown et al. (2019) suggests a merger age of ∼1.94 Gyr with at least one previous pericenter passage. We compare our high-resolution Chandra images of UGC 12491 and NGC 7618

in Figures 2 and 4, respectively, to the simulation density slice in the upper panel of Figure 6 to study the fine structure in the gas. We first compare the detailed morphology of the NGC 7618 and UGC 12491 merging cores to that seen in the simulated galaxies, and then compare the morphology of the tails.

4.1.1. Density Morphology in the Remnant Cores

The simulated galaxy to the southeast in Figure 6 shows features in the density slice similar to the observed X-ray surface brightness features in NGC 7618 shown in Figure 4 and the lower panel of Figure 7. The nose and northern edge in both the southeastern simulated galaxy and NGC 7618 show low-amplitude rolls or scallops, likely caused by hydrodynamic KHIs. Such KHIs are expected in inviscid gas. NGC 7618 and the southeastern simulated galaxy have a broad western wing with a boxy edge to the north. The bright plume in NGC 7618 is not as prominent in the southeastern simulated galaxy. Filamentary features are found in both the Chandra X-ray image of NGC 7618 and in the simulation slice, but in contrast to the observed filament that emerges from the nose of NGC 7618 near the plume, the filaments found in the southeastern simulated galaxy are north of the western wing along the line connecting the remnant cores. However, these turbulence-related plumes and filaments are thought to be transient features and exact matching of length and location should not be expected.

The simulated galaxy to the northwest in Figure 6 displays features similar to those observed in our high-resolution Chandra X-ray surface brightness images of UGC 12491 in Figure 2. UGC 12491 and the northwestern simulated galaxy each have a boxy North Wing feature. However, the observed edge in the North Wing of UGC 12491 is smoother than that in the northwestern simulated galaxy. A higher-density plume, directed from the galaxy's center toward its nose, is seen in the northwestern simulated galaxy. The plume is likely pushing gas outward, making the nose edge of the simulated galaxy irregular on scales of ∼20 kpc. This plume in the northwestern simulated galaxy is much more like the plume observed in NGC 7618. In UGC 12491 the central elongated dense gas is oriented nearly parallel to the nose, like a sloshing edge, and the observed irregularities at the nose edge are an order of magnitude smaller.

4.1.2. Gas Morphology of the Slingshot Tails

The observed tails in the Chandra X-ray surface brightness images of NGC 7618 and UGC 12491 are remarkably similar in morphology to the slingshot tails found in the simulation density slice of the merging southeastern and northwestern galaxies, respectively, at apogee. In the southeastern simulated galaxy, the tail extends southward from its western wing. This supports the hypothesis, presented in Section 3.2.2, that the outer part of the western wing in NGC 7618 (the West Wing2 region) is tail gas before the tail is seen to wind southward around the galaxy. In both NGC 7618 and the southeastern simulated galaxy, the tails extend to the south for ∼100 kpc before turning to the north and northeast. The inner edge of each tail winds close to its parent galaxy's eastern wing.

The simulated tails shown in Figure 6 are expansive with widths $\gtrsim$200 kpc after the tails bend back toward their parent cores. The outer edges of the tails remain well defined for

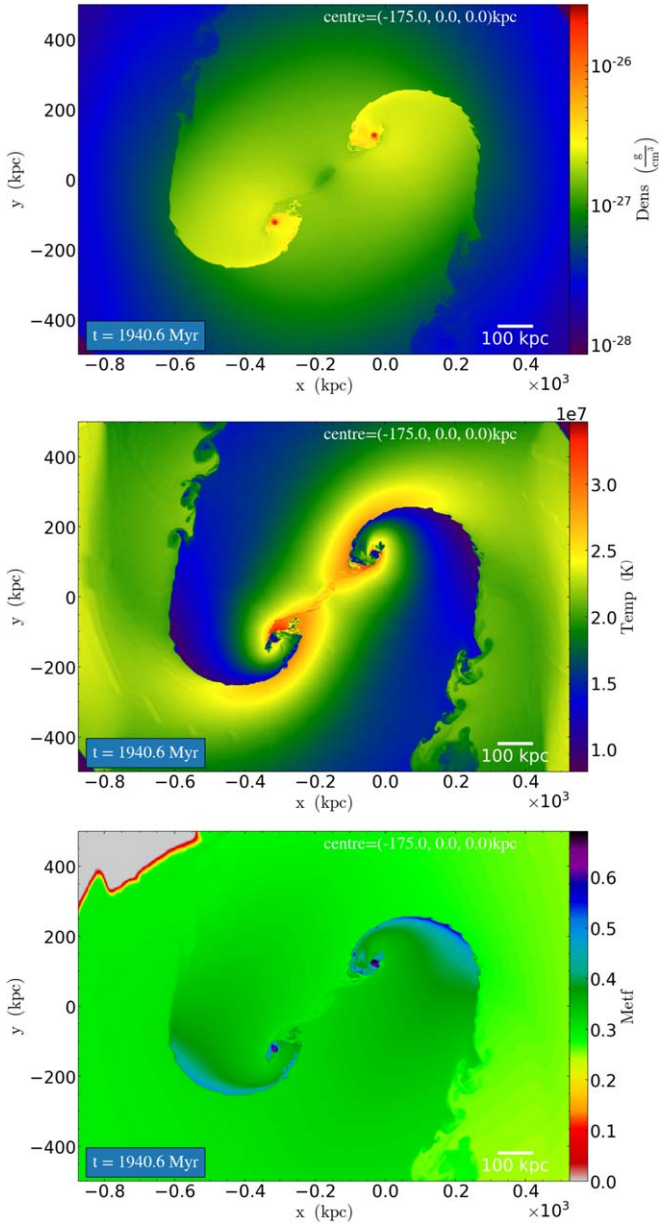

Figure 6. Slices at $z = 0$ from a numerical simulation of the merger of two equal-mass galaxy groups with masses roughly equal to those of the NGC 7618 and UGC 12491 galaxy groups showing hot gas density (upper), temperature (middle), and metallicity (lower) as the galaxy groups approach apogee after one pericenter passage.

>400 kpc along the length of the tail, while the gas density decreases by a factor ∼2. Note that such an extent is larger than the 8.′3 × 8.′3 (180 kpc × 180 kpc) ACIS S3 field of view (FOV) at the redshift of the NGC 7618/UGC 12491 system. The outer edge of NGC 7618's tail remains well defined along the observable length of the tail, i.e., until the outer edge of the tail falls outside the FOV of the combined observations (see Figure 1). While this general morphology of NGC 7618's tail is qualitatively similar to the morphology of the tail in the southeastern simulated galaxy, the observed width of the tail in NGC 7618, measured east from the remnant core is only half that found in the simulated tails. As pointed out by Sheardown et al. (2019), this may be at least partly due to a projection effect. If the merger plane is inclined relative to the LOS, the

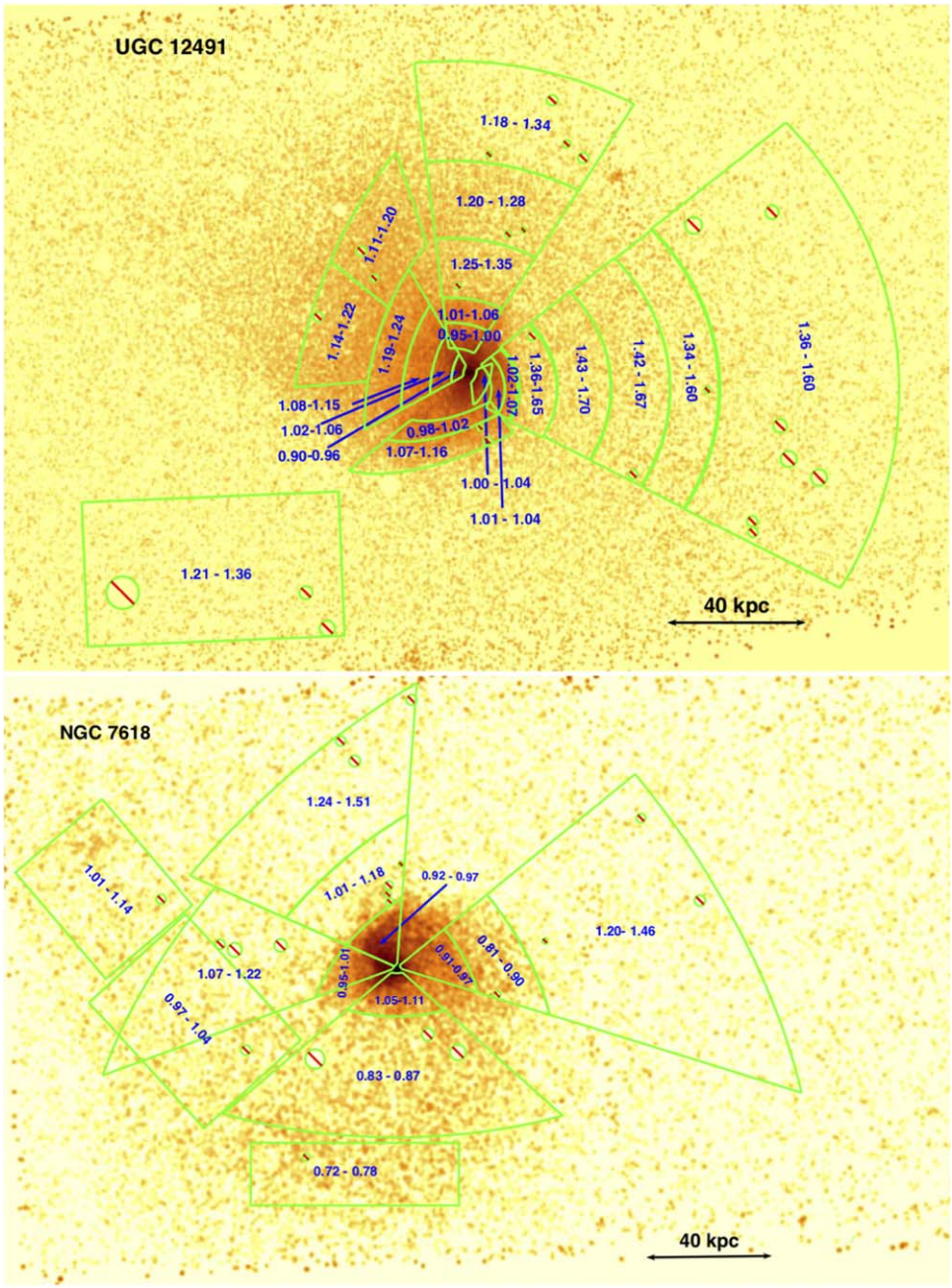

Figure 7. APEC spectral model 90% CL temperature ranges in kiloelectronvolt units superposed on 0.5–2 keV Chandra X-ray surface brightness images of UGC 12491 (upper panel, see Table 10 and Figure 2) and NGC 7618 (lower panel, see Table 5 and Figure 4). The scale 40 kpc = 1.′85 in each figure.

simulation tails appear narrower and more tightly wound (see Figure 7 in Sheardown et al. 2019).

The slingshot tail in the northwestern simulated galaxy in Figure 6 has two higher-density streams that make it appear bifurcated as it curves to the north after emerging from the remnant core's south wing. In Figures 1 and 2, we can see the same bifurcated morphology and bend to the north in the X-ray surface brightness images of UGC 12491's tail. The northwestern simulated galaxy's tail is tightly wound to the west and south around the galaxy core, such that the simulated gas density west of the core is higher than that to the southwest along the line joining the merging partners. A similar region of enhanced X-ray surface brightness corresponding to higher-density gas, that may be an extension of its tail, is found west of UGC 12491 as shown in Figure 1. However, the outer extent of this higher-density region to the west of UGC 12491 is more diffuse than the well-defined outer edge expected for the tail, and the width of the region is less than that expected from the simulation density slice.

Low-amplitude KHI rolls are seen along the outer edges of the tails in the southeastern and northwestern simulated galaxies. The amplitude of these KHIs grow as the distance along the tail increases and the gas density decreases. These KHIs at larger distances along the tails would be faint and difficult to detect in our data.

4.2. Temperature and Metallicity Comparisons

The simulated temperature and metallicity maps in the middle and lower panels of Figure 6 and the observed projected

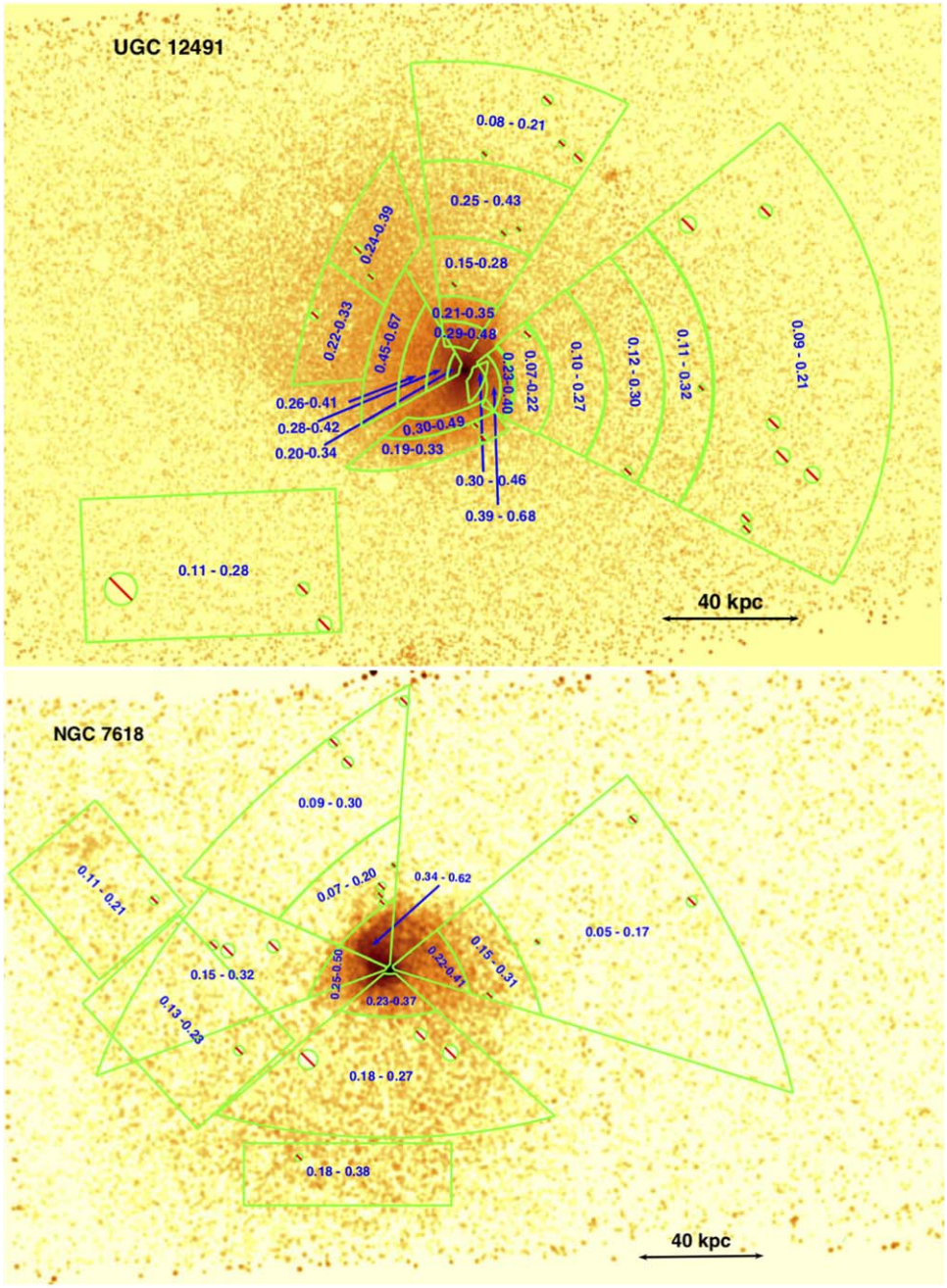

Figure 8. APEC spectral model 90% CL metallicity ranges in $Z_{\odot}$ units superposed on the 0.5–2 keV Chandra X-ray surface brightness images of UGC 12491 (upper panel, see Table 10 and Figure 2) and NGC 7618 (lower panel, see Table 5 and Figure 4). The scale 40 kpc = 1.′85 in each figure.

temperature and metallicity maps in Figures 7 and 8 show qualitatively similar, complex temperature and metal abundance structures. In the simulated temperature slice, gas heated by the merger interaction fills the space between the two galaxies and surrounds the cool galaxy gas cores, dense filaments, and extended boxy features. This is also seen in the observational data. From the best-fit APEC spectral models listed in Table 5 for UGC 12491 and in Table 10 for NGC 7618, the projected temperature for gas filling the space between UGC 12491 and NGC 7618, measured in the South IGM and West Wing3 regions, respectively, is higher (∼1.2–1.3 keV) and the metallicity is lower (0.1–0.2 $Z_{\odot}$) than in the cool (0.9–1.0 keV) merger cores, boxy features, and filaments that are composed of higher metallicity (∼0.3–0.4 $Z_{\odot}$) galaxy gas (see the Nose1,2, North Wing1,2, Inner W1,2, South Wing1 regions in the upper panels of Figures 7 and 8 and in Table 5 for UGC 12491 and the Head1, Plume1, East Wing1, and West Wing1 regions in the lower panels of Figures 7 and 8 and in Table 10 for NGC 7618).

The highest temperature gas in the simulation lies just outside the leading edges of the cool merger cores. In the southeastern simulated galaxy, the highest temperature gas extends ∼50 kpc to the north of the core, while the highest temperature gas outside the leading edge of the northwestern simulated galaxy is confined to a narrow (<10 kpc) region adjacent to the edge. Since the simulated galaxy groups are of equal mass, this difference in the morphology of the regions is likely an artifact of the viewing angle of the simulation slice

relative to the orbital plane of the merger. The highest temperature (1.4–1.7 keV) gas measured in the observed NGC 7618/UGC 12491 merger is found west of the leading edge of UGC 12491 (see the Nose3–7 regions in Table 5 and in Figure 7). This large high-temperature region is more like the high-temperature region found north of the leading edge of the southeastern simulated galaxy rather than the northwestern simulated galaxy, as might be expected from comparisons of gas morphology in Section 4.1. However, the high-temperature region observed west of UGC 12491 extends twice as far (∼100 kpc) from the leading edge as that of the highest temperature region in the southeastern simulated galaxy. Also the observed X-ray surface brightness, and thus gas density, west of UGC 12491, shown in Figure 1, is higher than that to the south of UGC 12491 between the merging cores, while in the southeastern simulated galaxy, the highest temperature gas is found in a region of lower density than that found elsewhere between the simulated cores. North of NGC 7618, we do not observe a significantly higher temperature region close to the leading edge, as one might expect from the simulated temperature slice. If the high-temperature region is narrow or contaminated with cool filaments of galaxy gas, as is the case for region Plume2 in NGC 7618, the limited photon statistics available for spectral analysis in NGC 7618 would make such a high-temperature (lower-density) region difficult to detect.

In the simulated merger, streamers of hot gas, displaced from the highest temperature regions in front of the leading edges of each galaxy by the close encounter, form a high-temperature, low-density bridge midway along the line connecting the two galaxy cores. As shown in Figure 6, this feature persists in the simulations even as the merging partners approach apogee. Since that region falls far from the aimpoints of our observations, it is not surprising that we find no evidence for such a high-temperature bridge in our data.

4.2.1. Temperature and Abundance Comparisons in the Tails

As discussed in Section 4.1.2 and seen in Figure 6, the tails in the simulation slices emerge from the West Wing for the southeastern galaxy and the South Wing for the northwestern galaxy. Hot gas with temperatures equal to that of gas between the merger cores follows the outer edge of the simulated tails from their apparent origin in the wings until the wide bend around their parent cores (see the middle panel of Figure 6). The $1.32^{+0.14}_{-0.12}$ keV temperature of gas measured in the West Wing3 region in NGC 7618 just outside the emerging tail in West Wing2 is consistent with this prediction.

The simulation temperature slice shows that in and near the western wing in the southeastern galaxy and the south wing in the northwestern galaxy, the distribution of gas within the tails is composed of smaller, irregular regions of different temperature gas. The temperatures in these irregular regions are intermediate between the temperature of the gas in the cool merger cores and the high-temperature gas between the merger cores and in front of their leading edges. Physically this may be the slingshot tail gas pushing past and being disturbed by the slowing remnant core as the core approaches apogee. In Figure 6, regions of multi-temperature gas within the tail are most apparent in the northwestern simulated galaxy, where these regions of different densities, temperatures, and abundances cause the tail to appear bifurcated. As discussed in Section 4.1.2, the Chandra X-ray image of the observed tail in UGC 12491 shows a similar morphology. In UGC 12491 the intermediate temperatures (∼1.2 keV) measured in the North Tail, South Tail, and Inner Tail E4 regions in UGC 12491 compared to 0.9–1.0 keV in the galaxy and the 1.3 keV gas between the cores (the South IGM region in Table 5) are qualitatively consistent with what one would expect for an average over such multi-temperature gas. The metal abundance in the Inner Tail E4 region is also significantly higher than that measured in the other tail regions (see the upper panel of Figure 8). Although regions of higher metallicity gas are expected in the tail, the lower panel of Figure 6 shows that, in the simulation metallicity slice, the regions with higher metal abundances are found near the outer edges of the tail, while in UGC 12491 the measured high metallicity region is on the tail's inner edge.

Farther from the wings, as the tail curves sharply around the galaxy, the temperature of the gas in the simulation decreases smoothly across the width of the tail from higher temperatures for gas on the inner (most tightly wound) edge of the tail to lower temperatures for gas on the outer edge of the tail. In the middle and lower panels of Figure 6, the lowest temperature, highest metallicity gas in each tail is comparable to the temperature and metallicity in the inner regions of the parent remnant core, and is found along the outer edge of the tail, along the final wide bend as the tail changes direction back toward its parent galaxy. In NGC 7618, we are able to trace the tail as it changes direction from trailing south of West Wing2 through its region of maximum curvature until it winds northeast back toward NGC 7618's core. As discussed in Section 3.2.2, the South Tail1,2 and Southern Most Tail regions measure temperatures across the width of the tail as it makes this change in direction, The decreasing temperatures measured from near the galaxy ($1.07^{+0.04}_{-0.02}$ keV in South Tail1) through the center of the tail ($0.83^{+0.02}_{-0.02}$ keV in South Tail2) to the tail's outer edge ($0.75^{+0.03}_{-0.03}$ keV in the Southern Most Tail) are consistent with the temperature gradient expected in this region from the simulations. After the tail has completed its turn to the northeast, the gas temperatures measured in the Mid Tail and North Tail regions in NGC 7618 average over the width of the tail. Thus, the measured intermediate temperatures ∼1 keV are also qualitatively consistent with the simulation.

5. Conclusions and Future Work

In this paper, we used Chandra X-ray observations to study the properties of hot gas in the major merger of the NGC 7618 and UGC 12491 galaxy groups, and compared our findings to simulations of a merger of two equal-mass galaxy groups roughly matched to the total mass, density and temperature profiles expected for the NGC 7618 and UGC 12491 galaxy groups. Gas in the simulations was assumed to have zero viscosity. X-ray spectra from our Chandra data are modeled using absorbed single-temperature APEC models throughout this study.

We find the following:

1. From 0.5–2 keV Chandra X-ray surface brightness images, we identified edges, wing-like and boxy features, filaments, and tightly wound tails in the hot gas of each galaxy group.
2. X-ray surface brightness profiles across features of interest contain multiple surface brightness discontinuities (edges) that are well characterized using spherically symmetric power-law models with a density contact

discontinuity at each edge. These edges are largely consistent with sloshing, as expected in merging systems.
3. Hot gas in the merger cores, boxy features, wings, and filaments have temperatures $\sim$1 keV and metallicities $\sim 0.3\,Z_{\odot}$.
4. Hot gas between NGC 7618 and UGC 12491 has a higher temperature ($\sim$1.3 keV) and lower metal abundance (~ 0.1–$0.2\,Z_{\odot}$) than within the merger cores. The highest temperature gas ($\sim$1.5–1.6 keV) is found west of UGC 12491's sharp edge.
5. Comparison of these observational results with simulations of an equal-mass merger of two galaxy groups roughly matched to NGC 7618 and UGC 12491 suggests that we are viewing the NGC 7618 and UGC 12491 groups at a merger age of $\sim$2 Gyr after one pericenter passage, when the galaxy groups are at the apogee of their orbits.
6. The striking qualitative similarities between these simulations using inviscid gas and our observations suggest that the observed hot gas in the NGC 7618/UGC 12491 merger has zero viscosity.
7. The observed tails are arc shaped and tightly wound about their respective merging cores, consistent with slingshot tails formed after a pericenter passage at a large impact parameter.
8. Spectral fits across NGC 7618's tail near maximum curvature show that the gas temperature decreases from the inner to the outer edge of the tail, consistent with that expected from simulations.

While the qualitative similarities between the observations and simulations are encouraging, differences still exist:

1. The observed tails in Figure 1 and Figures 4 and 2 appear narrower than those in the simulated density slice shown in Figure 6. However, simulations show that if the merger plane is not in the plane of the sky, i.e., the merger plane is rotated relative to the LOS, the simulated projected X-ray intensity of arc-shaped slingshot tails may appear narrower and more tightly bound than if the merger plane is in the plane of the sky (see Figure 7 in Sheardown et al. 2019). It is not clear whether the apparent narrow width of the observed slingshot tails for NGC 7618 and UGC 12491 can be reproduced in these simulations by simply varying the angle of the LOS relative to the merger plane for projected observables, or is an observational artifact of our limited statistics and ACIS-S FOV, or may point to additional physics important to the merger not included in existing simulations.
2. The highest temperature gas measured in our observations is located just west of the sharp Nose edge of UGC 12491. Simulations and our X-ray surface brightness image in Figure 1 suggest that the increased density west of UGC 12491 is an extension of UGC 12491's arc-shaped tail as it winds around its remnant core. However, simulations expect arc-shaped slingshot tails to be primarily composed of cool, unmixed galaxy gas, in contradiction to the high temperatures observed in that region. Thus the origin of this hot gas is unclear. Could this gas be heated (shocked) IGM gas rather than an extension of the tail? This latter interpretation may be more consistent with the measured high temperature in a region of higher gas density.
3. The NGC 7618 and UGC 12491 galaxy groups are of approximately the same mass. Simulations predict that the remnant parent cores develop tails of similar size and that appear symmetrical in projected X-ray intensity maps even if the merger plane is rotated relative to the LOS (Sheardown et al. 2019). However, NGC 7618's tail does not appear as tightly wound about its parent core as that of the tail about UGC 12491. This again may be a projection effect due to the orientation of the LOS relative to the plane of the merger. Alternatively, the observed asymmetry could possibly result from differences in the overall group potentials due to different ellipticities or size, despite similar masses, or reflect different interaction histories of the groups prior to this merger that might, for example, introduce different initial velocities of the groups prior to their first encounter. Such asymmetries would need to be reflected in the initial parameter space used to construct simulation models.

Given their low redshift, the merger of NGC 7618 and UGC 12491 may be the best example in the local universe of a major merger of two low-mass galaxy groups at apogee, and, thus, is deserving of further study. We note that the current simulations were only designed to provide sensible initial dark matter density, IGM density, and temperature profiles for a major merger of two galaxy groups similar to that of NGC 7618 and UGC 12491. They were not designed to quantitatively match the level of detail revealed by the current observations. Simulation studies that probe the origins of the differences discussed above, as well as the prevalence and resilience of turbulence-induced, transient features, such as the filaments, plumes, and bifurcated tails seen in these Chandra data, are interesting topics for future study.

Similarly, improved observations are needed to inform and test the simulation results. The ideal instrument for future observations should couple large effective areas at temperatures $\sim$1 keV with large FOV to map the full extent of the tails, measure density, temperature, and metallicity distributions throughout the tails and in the IGM between and around the dominant galaxies, and to identify the faint, large-scale KHI features predicted to form along a slingshot tail's outer edge. Detailed studies of the smaller-scale turbulence-induced features, such as filaments or plumes, and edge-like sloshing features associated with the merging cores would also require high ($\sim$arcsecond) spatial resolution. Such future simulation and observational studies will continue to sharpen our understanding of galaxy group merger dynamics and the microphysics of hot gas throughout the merging system during this important stage of structure formation.

Acknowledgments

This work was supported in part by NASA Chandra grant GO4-15082X, and by the Smithsonian Institution. J.T.W. gratefully acknowledges support from a Bill Davis SURF Fellowship. Data reduction and analysis were supported by the Chandra X-ray Center CIAO software and calibration database. The NASA/IPAC Extragalactic Database (NED), which is operated by JPL/Caltech, under contract with NASA was used throughout. We thank M. Markevitch for the surface brightness profile construction and analysis routines and L. Lovisari for useful discussions.

Appendix A
Profile Fitting across Multiple Edges

In this section, we present the spherically symmetric single- and multiple-edge density models used to fit X-ray surface brightness profiles for NGC 7618 and UGC 12491. We caution the reader that for regions outside the galaxy where the features show a complex morphology, spherical symmetry may not be a good approximation and these simple models may only provide a parameterization of the structure rather than a measurement of the physical, electron density profile. By parameterizing the complex structure in simulation data in the same way as the observational data, one can use the simulation to infer the unprojected three-dimensional electron density distribution of the hot gas.

For profiles with a single surface brightness discontinuity (edge) located at radius r_e and with jump j_e, the electron gas density model is given, moving inward from large radii, by

$$\begin{aligned}\tilde{n}_o(r > r_e) &= A\left(\frac{r}{r_e}\right)^{\alpha_o}\\ \tilde{n}_i(r < r_e) &= Aj_e\left(\frac{r}{r_e}\right)^{\alpha_i},\end{aligned} \tag{A1}$$

with A the normalization, $\alpha_o(\alpha_i)$ the density power-law indices outside (inside) the edge, r_e the location of the edge, and $j_e = \tilde{n}_i(r = r_e)/\tilde{n}_o(r = r_e)$ the jump (Vikhlinin et al. 2001). $\tilde{n}_x$ is a fit variable proportional to the electron density n_x and defined as $\tilde{n}_x = \sqrt{\Lambda_x} n_x$, $x = o$, i for outside and inside the edge, respectively. The surface brightness profile is fit by integrating the emissivity per unit area, $\tilde{n}^2(r)$, along the LOS for each r using a multivariate χ^2 minimization algorithm, allowing the edge location r_e, jump j_e, and power-law indices α_o and α_i to vary.

For multiple edges, we repeat this modeling for each edge requiring the power-law index to be the same between successive edges. However, we do not have sufficient statistics to fit all the variables at once, so we proceed iteratively from large radius to small. For two edges, we first fit the outermost edge with Equation (A1). Note that the power-law slope α_2 between the outer and inner edges depends sensitively on the fit to the inner edge and it, in turn, affects the best-fit value for the jump at the outer edge. Thus we freeze only the outer power-law slope α_3 and outer edge location r_{eo} from the first fit, but allow the outer jump j_o, power-law slope between the edges α_2, the inner edge location r_{ei} and jump j_i, and the inner power-law index α_1 to vary. We then refit the data from large to small radii using Equation (A2).

$$\begin{aligned}\tilde{n}(r > r_{eo}) &= A\left(\frac{r}{r_{eo}}\right)^{\alpha_3}\\ \tilde{n}(r_{ei} < r < r_{eo}) &= Aj_o\left(\frac{r_{ei}}{r_{eo}}\right)^{\alpha_2}\left(\frac{r}{r_{ei}}\right)^{\alpha_2}\\ \tilde{n}(r < r_{ei}) &= Aj_ij_o\left(\frac{r_{ei}}{r_{eo}}\right)^{\alpha_2}\left(\frac{r}{r_{ei}}\right)^{\alpha_1}.\end{aligned} \tag{A2}$$

This procedure is then iterated for additional edges. For these data, the maximum number of edges identified is three. Equations (A1) and (A2) are used to fit the outer and middle edges. The full set of model parameters are power-law indices α_i, $i = 1, 4$ with increasing integer for increasing radius, as in Tables 3 and 8, three edge locations and three associated jumps (r_{ex} and j_x, $x = o$, m, i for the outer, middle and inner edges, respectively. Fitting iteratively from large radii to small, r_{eo} and α_4 are fixed by the first iteration using Equation (A1) to fit the outer edge, j_o, r_{em}, α_3 by the second iteration fitting the outer two edges using Equation (A2). The final iteration then determines the remaining parameters (α_1, α_2, r_{ei}, j_i, j_m).

Appendix B
Definitions of Spectral Regions

In Tables 12 and 13 we define in detail the spectral regions shown in the lower panel of Figure 2 for the UGC 12491 galaxy group. All of the spectral regions other than the rectangular (box) region used to determine the temperature and abundance of the IGM to the south of UGC 12491 are elliptical panda regions, confined to the sectors also listed in Table 13. To measure the properties of the hot gas across the X-ray surface brightness discontinuities as cleanly as possible, we define a bounding ellipse that matches the shape of the surface brightness edges within the sector of interest. The bounding ellipses for the regions shown in Figure 2 are listed in Table 12. Note that the bounding ellipses for the tail regions and the Inner W region are each centered on the X-ray peak of UGC 12491, while the bounding ellipses for the Nose and North Wing are offset from that peak. In Table 13 we list the (semimajor, semiminor) radii for the inner and outer ellipses, each concentric to the bounding ellipse in Table 12, and that, when constrained to lie in the corresponding sector given in columns (4) and (5) of Table 13, complete the definition of the spectral regions shown in Figure 2. We also define the rectangular region used to measure the properties of the group gas south of UGC 12491 in the direction of the merging partner NGC 7618.

In Tables 14 and 15, we present similar data to define the spectral regions for NGC 7618 shown in the lower panels of Figure 4. In Table 14, we list the bounding ellipses used to construct the X-ray surface brightness profiles and the elliptical panda spectral regions. All of the bounding ellipses are centered at the X-ray/optical center ($\alpha = 23^{\rm h}19^{\rm m}47\overset{\rm s}{.}22$, $\delta = +42°51'\,09\overset{''}{.}5$) of NGC 7618. As in Table 13, the definition of the region is completed by listing the (semimajor, semiminor) axes of the inner and outer ellipses, concentric to the bounding ellipse, and constrained to lie in the angular sector that defines the elliptical panda segment. We use three rectangular regions to more precisely map the projected curved morphology of the outer tail. The centers in J2000 WCS coordinates, (length, width), and orientation angle of tail spectral regions are listed in Table 16.

Table 12
Bounding Ellipse Parameters for UGC 12491 Surface Brightness Profiles and Spectral Regions

Region	Center (R.A., Decl.)	a,b (arcsec, arcsec)	θ (deg)
(1)	(2)	(3)	(4)
Nose	$23^h18^m39.^s687$, $+42°57'15.''366$	56.1, 50.195	0
North Wing	$23^h18^m39.^s418$, $+42°57'18.''319$	56.172, 50.259	0
Inner W	$23^h18^m38.^s2$, $+42°57'29.''0$	21.55,12.1	254.8
Inner E Tail	$23^h18^m38.^s2$, $+42°57'29.''0$	21.55, 12.1	254.8
Outer Tail N	$23^h18^m38.^s2$, $+42°57'29.''0$	21.55,12.1	254.8
Outer Tail S	$23^h18^m38.^s2$, $+42°57'29.''0$	21.55, 12.1	254.8
South Wing	$23^h18^m38.^s253$, $+42°57'29.''145$	65.1, 28.494	27

Note. Column (2) lists the J2000 WCS coordinates of the ellipse center; column (3) lists the (semimajor, semiminor) axes of the bounding ellipse; and column (4) lists the position angle measured counterclockwise from west to the major axis of the ellipse.

Table 13
UGC 12491 Spectral Regions

Region	a_i,b_i (arcsec, arcsec)	a_o,b_o (arcsec, arcsec)	A (deg)	B (deg)
(1)	(2)	(3)	(4)	(5)
Nose1	33.474, 29.950	44.327, 39.661	333	38.2
Nose2	44.327, 39.661	56.100, 50.195	333	38.2
Nose3	56.100, 50.195	87.535, 78.321	333	38.2
Nose4	87.535, 78.321	129.865, 116.195	333	38.2
Nose5	129.865, 116.195	176.258, 157.704	333	38.2
Nose6	176.258, 157.704	216, 193.264	333	38.2
Nose7	216, 193.264	360, 322.107	333	38.2
North Wing1	33.474, 29.951	56.172, 50.259	57.2	96.75
North Wing2	56.172, 50.259	78.782, 70.489	57.2	96.75
North Wing3	78.782, 70.489	131.877, 117.996	57.2	96.75
North Wing4	131.877, 117.996	200.861, 179.718	57.2	96.75
North Wing5	200.861, 179.718	290.000, 259.474	57.2	96.75
Inner W1	9.0, 5.055	29.60, 16.625	276	22.4
Inner W2	29.60, 16.625	48.031, 26.976	276	22.4
Inner Tail E1	9.0, 5.055	24.654, 13.846	120.4	208.5
Inner Tail E2	24.654, 13.846	52.636, 29.562	120.4	208.5
Inner Tail E3	52.636, 29.562	90.925, 51.067	120.4	208.5
Inner Tail E4	90.925, 51.067	139.483, 78.339	120.4	208.5
Outer Tail N	139.483, 78.339	239.284, 134.391	108.4	141.3
Outer Tail S	139.483, 78.339	239.284, 134.391	141.3	184.8
South Wing1	65.100, 28.494	92.44, 40.461	219.2	305.8
South Wing2	92.44, 40.461	135.540, 59.326	219.2	305.8
South IGM[a]	205, 115.3	…	…	…

Note. Definitions of the spectral regions shown in the lower panel of Figure 2. For each elliptical panda segment, column (2) (a_i, b_i) and column (3) (a_o, b_o) give the inner and outer (semimajor, semiminor) axes of the inner and outer ellipses, respectively, concentric to the bounding ellipse given in Table 12. The spectral region is constrained to lie in the sector measured from angle A (column (4)) to angle B (column (5)). All angles are measured counterclockwise from west. *a* South IGM is a rectangular region centered at J2000 WCS coordinates $\alpha = 23^h18^m56.84^s$, $\delta = +42°54'.51.''75$ with (length, width) in column (2) and orientation angle $2.^\circ32$ measured counterclockwise from west to the length axis.

Table 14
Bounding Ellipse Parameters for NGC 7618 Surface Brightness Profiles and Spectral Regions

Region	a,b (arcsec, arcsec)	θ (deg)
(1)	(2)	(3)
Head	60.496, 46.996	51
North Plume	96.51, 46.0	44.64
West Wing	94.367, 53.762	309.65
East Wing	96.510, 46.00	44.64
South Tail	86.388, 43.194	0

Note. Each bounding ellipse is centered at WCS coordinates $\alpha = 23^{h}19^{m}47\overset{s}{.}22$, $\delta = +42°51'09\overset{''}{.}5$, coincident with the X-ray peak (and optical center) of NGC 7618. Column (2) lists the (semimajor, semiminor) axes of the bounding ellipse. Column (3) lists the position angle measured counterclockwise from west to the major axis of the ellipse.

Table 15
NGC 7618 Elliptical Panda Spectral Regions

Region	a_i,b_i (arcsec, arcsec)	a_o,b_o (arcsec, arcsec)	A (deg)	B (deg)
(1)	(2)	(3)	(4)	(5)
Head1	5.0, 3.884	60.5, 47.0	53.4	146.4
Head2	60.5, 47.0	200.0, 155.372	53.4	146.4
Plume1	5.0, 2.383	96.51, 46.0	85.7	155.8
Plume2	96.51, 46.0	213.251, 101.643	85.7	155.8
Plume3	213.251, 101.643	396.040, 188.8	85.7	155.8
East Wing1	5.0, 2.383	96.51, 46.0	155.9	200.0
East Wing2	96.51, 46.0	348.1, 165.9	155.9	200.0
West Wing1	4.958, 2.825	94.367, 53.762	342.65	39
West Wing2	94.367, 53.762	179.09, 102.03	342.65	39
West Wing3	179.09, 102.03	475.0, 270.614	342.65	39
South Tail1	10.0, 5.0	86.388, 43.194	220	318
South Tail2	86.388, 43.194	300.0, 150.0	220	318

Note. Definitions of the spectral regions shown in the lower panel of Figure 4. Column (2) (a_i, b_i) and column (3) (a_o, b_o) give the inner and outer (semimajor, semiminor) axes of the inner and outer ellipses, respectively, for each elliptical panda segment concentric to the bounding ellipse given in Table 14. The spectral region is constrained to lie in the sector measured from angle A (column (4)) to angle B (column (5)). All angles are measured counterclockwise from the west.

Table 16
NGC 7618 Rectangular Tail Spectral Regions

Region	Center (R.A., Decl.)	l,w (arcsec,arcsec)	θ (deg)
(1)	(2)	(3)	(4)
Southern Most Tail	$23^{h}19^{m}50\overset{s}{.}598$, $+42°48'06\overset{''}{.}984$	183.5, 55.3	359.9
Mid Tail	$23^{h}20^{m}03\overset{s}{.}417$, $+42°50'21\overset{''}{.}839$	150.584, 115.63	132.4
North Tail	$23^{h}20^{m}10\overset{s}{.}733$, $+42°52'18\overset{''}{.}688$	123.16, 100.4	310.3

Note. Rectangular spectral regions shown in Figure 4 used to measure the properties of hot gas in the outer tail regions of NGC 7618. Column (2) lists the center of the rectangular region in J2000 WCS coordinates, column (3) lists the (length, width) of the region, and column (4) lists the orientation angle of the rectangular region measured counterclockwise from west to the length axis.

ORCID iDs

M. E. Machacek https://orcid.org/0000-0002-0018-2129
C. Jones https://orcid.org/0000-0003-2206-4243
R. P. Kraft https://orcid.org/0000-0002-0765-0511
W. R. Forman https://orcid.org/0000-0002-9478-1682
A. Sheardown https://orcid.org/0000-0002-0543-7143

References

Anders, E., & Grevesse, N. 1989, GeCoA, 53, 197
Arnaud, K. A. 1996, in ASP Conf. Ser. 101, Astronomical Data Analysis Software and Systems V, ed. G. Jacoby & J. Barnes (San Francisco, CA: ASP), 17
Ascasibar, Y., & Markevitch, M. 2006, ApJ, 650, 102
Botteon, A., Gastalderllo, F., Brunetti, G., & Dellacasa, D. 2016, MNRAS, 460, L84
Bourdin, H., Mazzotta, P., Markevitch, M., et al. 2013, ApJ, 764, 82
Colbert, J. W., Mulchaey, J. S., & Zabludoff, A. I. 2001, AJ, 121, 808
Condon, J . J., Cotton, W. D., & Borderick, J . J. 2002, AJ, 124, 675
Crook, A. C., Huchra, J. P., Martimbeau, N., et al. 2007, ApJ, 655, 790
Crook, A. C., Huchra, J. P., Martimbeau, N., et al. 2008, ApJ, 685, 1320
Dasadia, S., Sun, M., Sarazin, C., et al. 2016, ApJL, 820, L20
David, L. P., Jones, C., Forman, W., et al. 2009, ApJ, 705, 624
De Breuck, C., Van Breugel, W., Röttgering, H. J. A., & Miley, G. 2000, A&AS, 143, 303
De Grandi, S., Eckert, D., Molendi, S., et al. 2016, A&A, 592, A154
Dickey, J. M., & Lockman, F. J. 1990, ARA&A, 28, 215
Eckert, D., Gaspari, M., Owers, M. S., et al. 2017, A&A, 605, A25
Forman, W., Churazov, E., Giacintucci, S., et al. 2010, in AIP Conf. Proc. 12148 (San Francisco, CA: ASP), 273
Gastaldello, F., Buote, D. A., Temi, P., et al. 2009, ApJ, 693, 43
Gastaldello, F., Di Gesu, L., Ghizzardi, S., et al. 2013, ApJ, 770, 56
Goulding, A. D., Greene, J. E., Ma, C.-P., et al. 2016, ApJ, 826, 167
Hallman, E. J., Alden, B., Rapetti, D., et al. 2018, ApJ, 859, 44
Hallman, E. J., & Markevitch, M. 2004, ApJ, 610, 81
Huchra, J. P., & Geller, M. J. 1982, ApJ, 257, 423
Huchra, J. P., Lucas, M., Masters, K. L., et al. 2012, ApJS, 199, 26
Huchra, J. P., Vogeley, M. S., & Geller, M. J. 1999, ApJS, 121, 287
Johnson, R. E., ZuHone, J., Jones, C., Forman, W. R., & Markevitch, M. 2012, ApJ, 751, 95
Kraft, R. P., Forman, W. R., Jones, C., et al. 2011, ApJ, 727, 41
Kraft, R. P., Jones, C., Nulsen, P. E. J., & Hardcastle, M. J. 2006, ApJ, 640, 762
Kraft, R. P., Roediger, E., Machacek, M., et al. 2017, ApJ, 848, 27
Kreisch, C. D., Machacek, M. E., Jones, C., & Randall, S. W. 2016, ApJ, 830, 39
Machacek, M., Dosaj, A., Forman, W. R., et al. 2005, ApJ, 621, 663
Machacek, M., Jones, C., Forman, W. R., & Nulsen, P. 2006, ApJ, 644, 155
Machacek, M. E., Jerius, D., Kraft, R. P., et al. 2011, ApJ, 743, 15
Machacek, M. E., O'Sullivan, E., Randall, S. W., Jones, C., & Forman, W. R. 2010, ApJ, 711, 1316
Markevitch, M. 2002a, arXiv:astroph/0205333
Markevitch, M., Gonzalez, A., & David, L. 2002b, ApJL, 567, L27
Markevitch, M., & Vikhlinin, A. 2007, PhR, 443, 1
Mitsuishi, I., Sasaki, S., Katsuhiro, H., et al. 2014, MmSAI, 85, 388
O'Sullivan, E., David, L., & Vrtilek, J. 2014, MNRAS, 437, 730
O'Sullivan, E., Schellenberger, G., Burke, D. J., et al. 2019, MNRAS, 488, 2925
Paterno-Mahler, R., Glanton, E. L., Randall, S. W., & Clarke, T. E. 2013, ApJ, 773, 114
Poole, G. B., Fardal, M. A., Babul, A., et al. 2006, MNRAS, 373, 881
Randall, S., Nulsen, P., Forman, W. R., et al. 2008, ApJ, 688, 208
Randall, S. W., Jones, C., Kraft, R., et al. 2009, ApJ, 696, 1431
Revnivtsev, M., Churazov, E., Sazanov, S., Forman, W., & Jones, C. 2008, A&A, 490, 37
Roediger, E., Kraft, R. P., Machacek, M. E., et al. 2012a, ApJ, 754, 147
Roediger, E., Lovisari, L., Dupke, R., et al. 2012b, MNRAS, 420, 3632
Roediger, E., Kraft, R. P., Nulsen, P. E. J., et al. 2015a, ApJ, 806, 103
Roediger, E., Kraft, R. P., Nulsen, P. E. J., et al. 2015b, ApJ, 806, 104
Roediger, E., Kraft, R. P., Nulsen, P., et al. 2013, MNRAS, 436, 1721
Russell, H. R., Fabian, A. C., McNamara, B. R., et al. 2014, MNRAS, 444, 629
Scharf, C. A., Zurek, D. R., & Bureau, M. 2005, ApJ, 633, 154
Sheardown, A., Fish, T. M., Roediger, E., et al. 2019, ApJ, 874, 112
Sheardown, A., Roediger, E., Su, Y., et al. 2018, ApJ, 865, 118
Smith, R. J., Lucey, J. R., Hudson, M. J., Schlegel, D. J., & Davies, R. L. 2000, MNRAS, 313, 469
Su, Y., Kraft, R. P., Nulsen, P. E. J., et al. 2017a, ApJ, 835, 19
Su, Y., Kraft, R. P., Roediger, E., et al. 2017b, ApJ, 834, 74
Verner, D. A., Ferland, G. K., Korista, K. T., & Yakovlev, D. G. 1996, ApJ, 465, 487
Vikhlinin, A., Markevitch, M., & Murray, S. S. 2001, ApJ, 551, 160
Voges, W., Aschenbah, B., Boller, T., et al. 1999, A&A, 349, 389
Wood, R. A., Jones, C., Machacek, M. E., et al. 2017, ApJ, 847, 79
Wright, E. L. 2006, PASP, 118, 1711
ZuHone, J. A., Markevitch, M., & Johnson, R. E. 2010, ApJ, 717, 908
ZuHone, J. A., Markevitch, M., & Lee, D. 2011, ApJ, 743, 16
ZuHone, J. A., Markevitch, M., Ruszkowski, M., & Lee, D. 2013, ApJ, 762, 69